VOLATILE ICE DEPOSITS IN LUNAR POLAR REGIONS AND THEIR SOURCES

Jasmeer Sangha

A THESIS SUBMITTED TO THE FACULTY OF GRADUATE STUDIES IN PARTIAL FULFILLMENT OF THE REQUIREMENTS FOR THE DEGREE OF MASTER OF SCIENCE

GRADUATE PROGRAM IN THE DEPARTMENT OF PHYSICS AND ASTRONOMY

YORK UNIVERSITY
TORONTO, ONTARIO

2018

Abstract

An amalgamation of code adapted from Schorghofer [2014] and Moores [2016] was used to simulate the movement of volatiles on the present-day surface of the Moon. The trapping of volatiles in permanently shadowed regions (PSRs) near the rotational poles was explored using a combination of numerical models of ballistic transport of water vapour. This process included both a validated Monte Carlo model and a full lunar exospheric model, which had not previously been used to explore poleward of 85°S or in any part of the northern hemisphere. This work predicts that 5.3% ±0.1 of water deposited on the surface of the Moon will be trapped in PSRs. Moreover, the transit times of lunar volatiles to high latitudes and the non-existence of large PSRs in low latitudes create the ideal environment for the largest concentrations of water ice to be found between 83° and 86° latitude, as we see on the lunar surface today. Despite the differences in PSRs available, volatile concentrations follow similar trends in both hemispheres and tend to peak approximately 5° from the poles. These results are produced without the use of the true polar wander theory. In addition to analysing water transport, this work simulates other volatiles observed in the LCROSS impact ejecta plume (H_2S, CO_2, NH_3, CH_3OH, C_2H_4). Analysis of volatile species simulations suggest photodissociation rates dominate trapping efficiency results.

Dedication

For my late brother, Kashmir.

Acknowledgements

I would like to extend my thanks to my supervisor, Dr. John Moores, without his constant guidance over the last two years the completion of this undertaking would not have been possible. His passions for leading, educating and discovering are unwavering and infectious.

I would like to acknowledge Dr. Norbert Schorghofer for his contribution of time and expertise regarding the subject matter of this thesis. The privilege to always have an open channel to discuss how to implement physical processes properly into my code is invaluable.

Thank you to the Planetary Volatiles Laboratory for their support. I would like to especially thank Christina Smith, Casey Moore, and Jacob Kloos for their advice regarding this thesis.

Finally, thank you to my friends and family that ensured the pressure to succeed never diminished.

Table of Contents

List of Tables

List of Figures

Chapter 1

Introduction

1.1 The Earth-Moon System

The origin of the Earth-Moon system has been studied extensively due to their unique relationship. The Earth and Moon have similar chemical compositions and are hypothesized to have been created from the same source material [Lugmair and Shukolyukov, 1998]. Through numerical simulations, it has been determined that a large-scale impact event or events had to have taken place to recreate the present-day Earth-Moon system [Hartmann and Davis, 1975][Benz, Slatttery and Cameron, 1986][Agnor Canup and Levison, 1999]. These studies suggest that an impactor ranging from a Mars-sized body to multiple smaller impactors could, by conservation of angular momentum, satisfy initial conditions needed to produce the Earth-Moon system we see today. A currently undetermined mass collided with the fast spinning protoplanetary Earth [Canup and Asphaug, 2001][Canup, 2008] and the debris from the impact collected into the two bodies we know today. Such violent collisions would necessarily disturb any volatiles on either body. It was thus widely believed that the lunar surface was void of any water following its origin

[Albarède ,2009][Taylor, Taylor, and Taylor, 2006]. However, Saal has shown through secondary-ion mass spectrometry of lunar samples, a process in which ions are projected at a surface which will eject surface material that can be analyzed, volatiles are present in basalts on the Moon's surface [Saal, et al., 2008]. Basalts in the form of volcanic glasses are the surface remnants of active volcanic periods in the Moon's past. Much like Earth, any water that could appear on the surface would need to be ejected by volcanism, deposited by impacts of carbonaceous chondrites, comets and solar wind implantation [Greenwood, et al., 2011][Boyce, et al., 2010].

There are areas known to be permanently shadowed regions (PSRs) where water ice can be trapped [Crovisier, 1989][Watson, Murray, and Brown, 1961a]. Lunar PSRs exist due to the combination of the satellite's orbital obliquity (6.68°) coupled with its inclination angle (5.15°) resulting in a difference of 1.53° between the ecliptic and its own rotational axis [Watson, Murray, and Brown, 1961b].

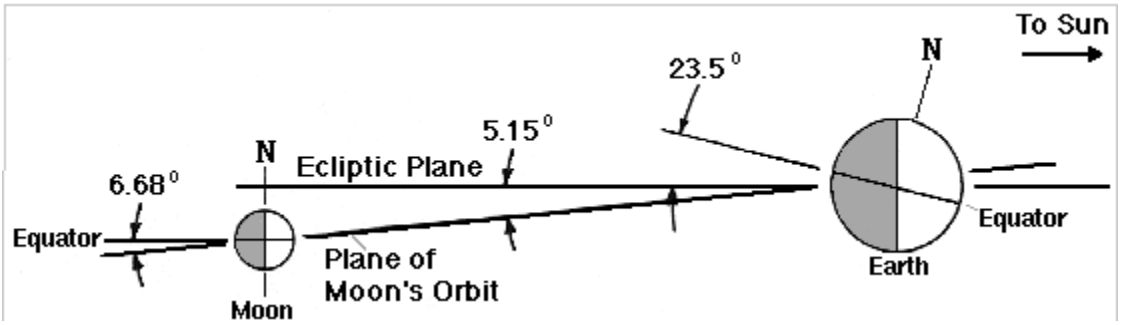

Figure 1.1.1: Diagram of the Earth-Moon system. Note the tilt of the Moon's equator in reference to its orbital plane. The coupling of these two phenomena allow for polar PSRs.

Particles that are exposed to solar radiation are cleaved apart by virtue of the photons exceeding the bond energy between atoms [Meeus, 1997]. Due to the Moon's virtually non-existent magnetic field, particles are under constant bombardment of high energy photons leading to a water photodissociation rate of $1.26\,x\,10^{-5}$ molecules per second: on average a 22 hour

lifetime before photodissociation occurs [Crovisier, 1989]. Though the Sun remains a source of ionized hydrogen, in the form of solar winds, which can combine with hydroxyl compounds to create water on the surface [Sunshine, et al., 2009], the Sun's UV rays carry enough energy to break down compounds. Photodissociation, similar to photoionization, is characterized as the absorption of photons resulting in the break down of molecules. The reactions this work is concerned with are characterized by:

$$H_nA + h\upsilon \longrightarrow H^+ + H_{n-1}A^-$$

This process, photodissociation, only occurs when particles are exposed to direct sunlight as a result, dark areas become an area of interest. PSRs are completely void of solar radiation, therefore inherently dark, and have temperatures which fall 60 K below water's volatility threshold, allowing PSRs to act as cold traps where water freezes and stays adsorbed to the surface [Paige, et al., 2010]. Signals of water ice near the lunar poles have been inferred through neutron spectroscopy [Feldman, et al., 1998][Mitrofanov, et al., 2010][Mitrofanov, et al., 2012]. The Lunar Exploration Neutron Detector (LEND) instrument aboard the Lunar Reconnaissance Orbiter (LRO) is able to measure neutron flux from particular regions. With the bombardment of photons from space, neutrons in the lunar subsurface can escape. The primary suppressor of the surface's neutron flux are hydrogen compounds. When observing PSRs, there was a notable decrease in neutron flux which implies the presence of hydrogen, possibly in the form of water ice. Furthermore, reflectivity of Lyman-alpha [Gladstone, et al., 2012] and ultraviolet albedo spectra [Hayne, et al., 2015] showed higher than expected values: suggesting surface ice in polar regions was reflecting excess amounts of energy back.

Cabeus crater is one of many low-lying areas encircled by higher topography near the Moon's poles which exhibited a high probability of containing water ice from the aforementioned

experiments. Cabeus is a crater with a 10 km radius which is located 5.5° from the south pole of the Moon. Following the work done by Chandrayaan-1 [Sridharan, et al., 2010], it was proposed that an impact in a PSR would allow measurements of the surface material to be taken. The plan, which was successfully executed, was to allow the upper stage of the Lunar Crater Observation and Sensing Satellite (LCROSS), Centaur, to impact Cabeus crater, a potentially volatile rich PSR. The ejecta plume created by the impact was analyzed as the Shepherding Spacecraft flew through it as it plummeted towards the surface. LCROSS confirmed water and hydroxyl signatures in the impact debris of Cabeus crater [Colaprete, et al., 2010].

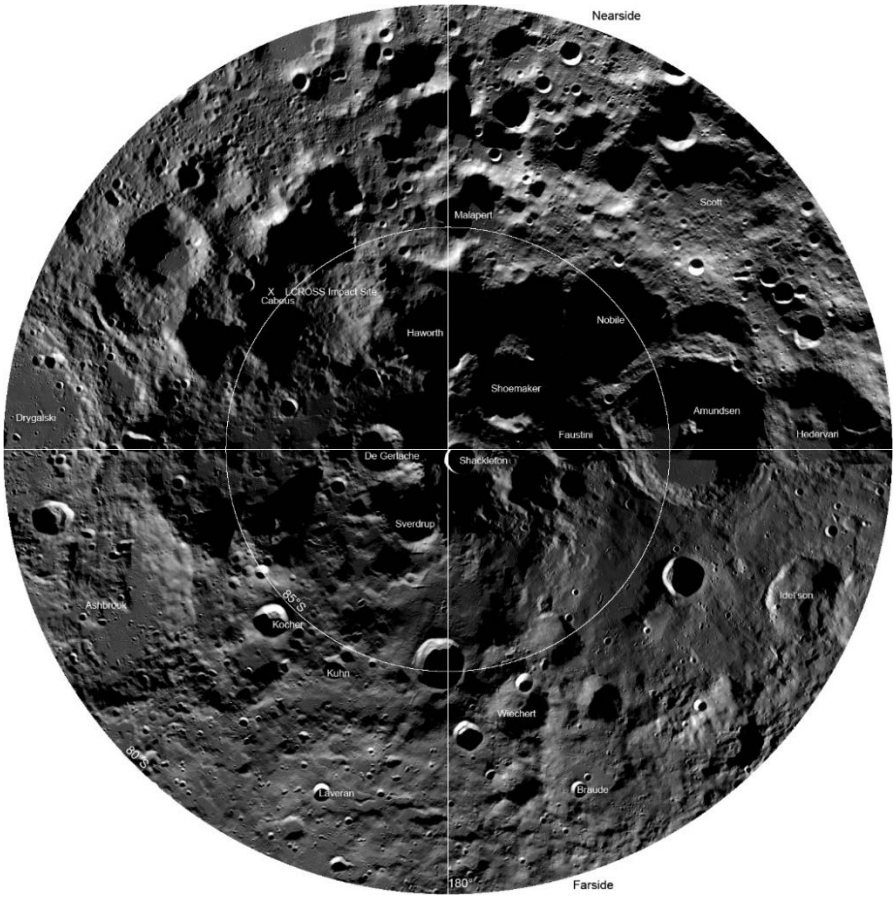

Figure 1.1.2: Wide Angle Camera Mosaic of the South pole (643 nm). Locations of interest are labelled. Cabeus and the LCROSS impact reside in the top left quadrant near the 5° line of latitude.

1.2 True Polar Wander

It has been proposed that True Polar Wander (TPW) is the mechanism that displaced the major ice deposits from the rotational poles [Siegler, et al., 2016]. The theory of TPW suggests water collects at the poles similar to what we see on Earth and Mars: high concentrations at the rotational poles which gradually decrease the closer one gets to the equator. The model proposed a mechanism that allows concentrations of water ice to be located away from the present rotational poles but needs work. For instance, this model assumes any incoming volatile deposits, post-inertia shift, would be insignificant compared to the water ice deposits that were already present before the shift. If this stipulation is not valid, one should see most of ice in the coldest regions i.e., in PSRs near the rotational poles. A major shift in mass distribution, such as the volcanism that led to Procellarum KREEP Terrane (PKT) at least 3.5 billion of years ago [Jacobsen, et al., 2010], would change the principal axis of rotation. TPW, illustrated in Figure 1.1.1, is the result of a shift in the inertia tensor – the mathematical object which describes linear relations of vectors, in this case the torques used to define a body's rotation. According to Siegler, this would explain why Cabeus has a particularly high concentration of water ice compared to other PSRs closer to the present rotation axis.

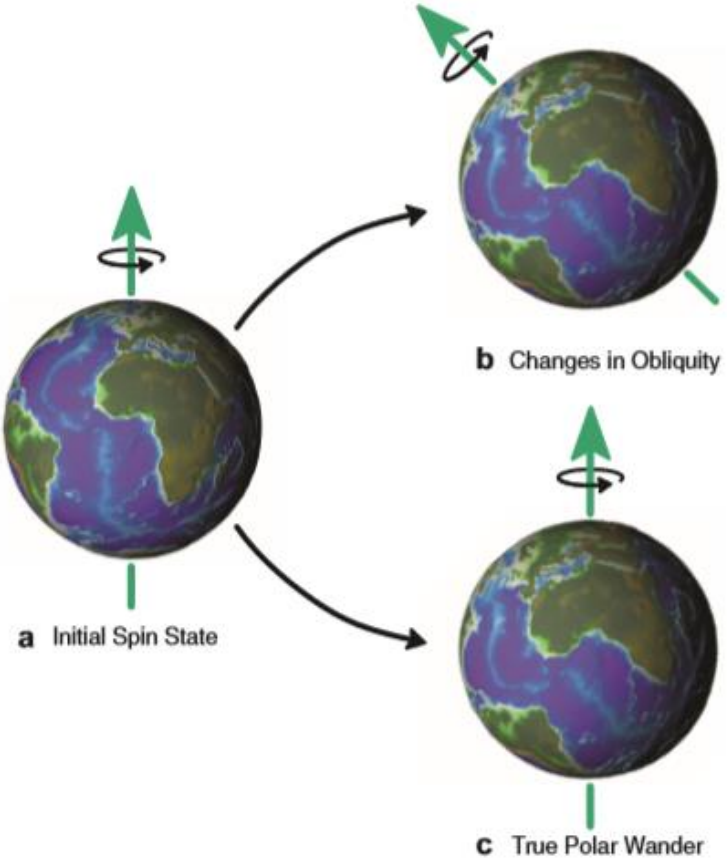

Figure 1.2.1: From Siegler et al., 2016, **a** represents an initial spin state. **b** shows a change in obliquity: axis of rotation unchanged relative to body**. c** shows TPW: rotation axis unchanged relative to system. Note the differences between cases **b** and **c**, the former changes the orientation of the rotational axis whereas the latter changes the position of the axis.

Additionally, there are other methods that can cause ice to be more highly concentrated away from the rotational poles. Moores [2016] showed that the cold temperatures of the south polar region create potential energy barriers for incoming particles, much like rain shadows seen on Earth. Lower latitude craters would have higher concentrations because particles trapped in PSRs could never gain enough thermal energy to hop back out. Additionally, Siegler assumes that the water ice present in these cold traps was accumulated prior to the volcanism, any deposits post-

PKT would need to be inconsequential relative to prior deposits which necessarily are billions of years old.

The old ice theory from Siegler's work is an issue because any new water deposited on the lunar surface would create new icy poles along side the displaced poles from TPW. One only needs a large enough source of water; i.e. asteroid impacts or solar wind implantation [Sunshine, et al., 2009], that is active after the PKT formation to create a plausible theory.

1.3 Exospheric Models

Ballistic hopping of particles on the lunar surface through a transient exosphere has been thoroughly researched and can transport water ice from place to place on the satellite's surface [Butler, 1997] [Schorghofer, 2014]. A transient exosphere is a fluctuating atmosphere on small bodies. The incoming heat sublimates ice on the surface during the day adding to the active atmosphere which will diminish at night as the temperature decreases and volatiles once again freeze onto the surface. This differs from our atmosphere which is denser and exhibits collisional processes.

Previously, exospheric models have been used to assess particle trapping percentage as a function of latitudinal distance from the poles [Schorghofer, 2014]. That work has yielded a more gradual diffusion pattern compared to work done by Moores [2016], which differs most notably by looking at true PSRs in the south polar region, restricting particles to only hop during the day, assumes a sinusoidal scaling relation for the surface temperature profile, and uses an exponential curve when determining a particle's photodissociation probability (compared to a linear one used

by Schorghofer, 2014). By adapting Schorghofer's model to take into consideration the polar PSRs identified by McGovern, et al., 2013, we can compare the results of previous work for the south and take a first look at trapping in the north. Results will be obtained from simulations of the migration of water particles on the Moon's surface in order to study the relative distribution in PSRs less than 10° from either pole. They will be generated using an adaptation of the exospheric model used by Schorghofer, 2014.

Furthermore, the same model will be applied to a subset of other lunar volatiles found by the LCROSS mission, namely: hydrogen sulfide (H_2S), carbon dioxide (CO_2), ammonia (NH_3), methanol (CH_3OH), and ethene (C_2H_4). By comparing the trapped concentration of the various volatiles to the observed values, one can estimate the concentrations of the initial populations that were deposited on the Moon.

Chapter 2

Background Information

2.1 Permanently Shadowed Regions

Permanently shadowed regions (PSRs) are a product of the Moon's inclination and orbital obliquity effectively cancelling each other out, that is to say the angle between the Moon's equator and the ecliptic is approximately 1.535°. This small angle results in permanently shadowed regions in high latitudes. Due to topographical variance on the surface on the Moon, some low-lying areas are in shadow all year long. The south pole sits inside the South pole – Aitken Basin, shown in Fig 2, a massive crater due to an impact approximately 4 billion years ago. The basin is surrounded by higher topography and additionally filled with newer craters that created the ideal conditions for PSRs. From this one can expect that PSRs cover more overall surface area by the south pole compared to the northern hemisphere, shown in Fig 3.

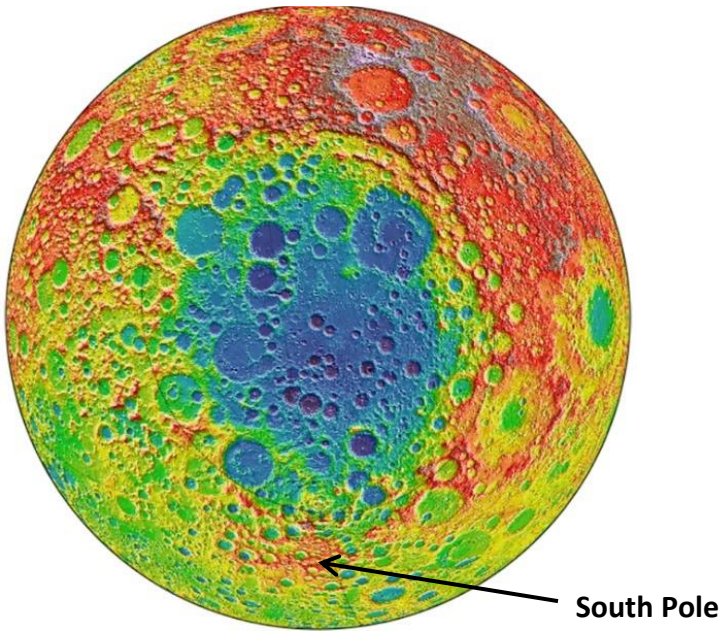

Figure 2.1.1: Topographical map of the lunar south pole from LOLA. Blue areas represent low elevation. Notice the high topography surrounding the basin which, along with the Moon's orbital parameters, help restrict solar flux into the area.

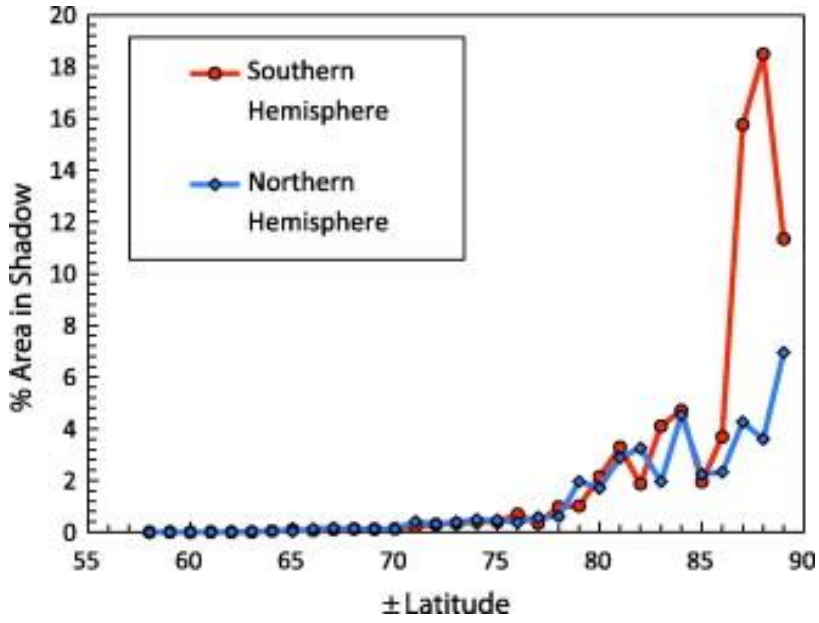

Figure 2.1.2: From McGovern, et al., 2013, absolute latitude versus % area covered in permanent shadow. Note the Southern hemisphere is dominant due to its low-lying topography. This information can be used to create a probability function for particles to be captured by PSRs instead of identifying hundreds of tiny traps.

2.2 Surface Temperature Profile

The driving force behind volatile transport on the lunar surface is the heat absorbed from the Sun. As the surface temperature increases, volatiles previously frozen on the surface sublimate and hop in a random direction. Using this process, we can simulate two things: the size and timing of jumps. Since particles near the equator are sitting on warmer regolith they absorb more energy and experience larger jumps. Jumps vary from $10^2 – 10^7$ m in length, refer to Figure 2.2.1. This is the crux for the theory behind ballistic transport of volatiles being the major factor pertaining to why more ice is found a couple degrees away from the pole than at it: hops decrease in length as particles approach the poles which makes it harder to reach traps extremely close to the poles. Additionally, since hopping is temperature dependent the vast majority of hopping occurs during the day. Notably, Schorghofer, 2014 showed that the majority of jumps happen at dawn due to the cold temperatures of the night not supplying enough energy for water to sublimate off of the surface. Once a sufficient temperature has been reached after sunrise, particles can sublimate off of the surface. Thus, it is to be assumed that particles rarely hop at night and Moores, 2016 takes advantage of this assumption by skipping nights for simulated particles saving on run time. Moores, 2016 also generates a global temperature profile by scaling Vasavada's equatorial temperature model [Vasavada, et al., 2012] as

$$T = T_{eq}\sqrt[4]{sin(\theta_d)} \tag{5}$$

Here T_{eq} is equatorial temperature and θ_d, is the declination. This method saves on computational speed but is a simple scaling relation of the equatorial temperature which breaks down in the polar

regions where the majority of this work focuses. Instead, this work chooses to generate a total temperature profile, as specified by Schorghofer, detailed in Section 4.2, which can be checked against Vasavada's equatorial model for validation [Schorghofer, 2014].

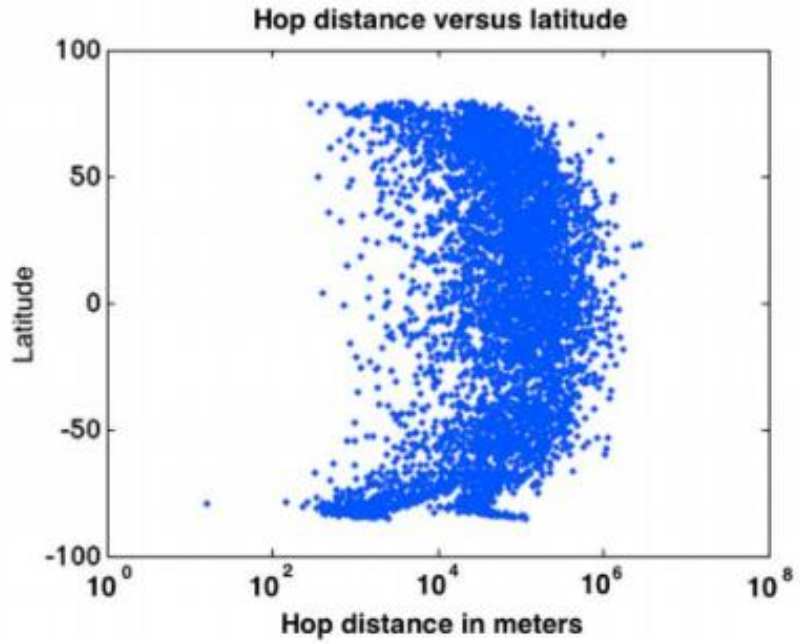

Figure 2.2.1: Figure 1c from Moores, 2016 showing hop distance as a function of latitude and more specifically surface temperature.

Chapter 3

Methods

3.1 PSR Implementation

In this work, traps are approximated as circular regions located no more than 10° from the North pole, or 6° from the south pole. For consistency, southern traps are identical, in geographic location and size, to those in Moores, 2016, a subset of the best candidates defined by Paige et al., 2010. The South polar traps extended as far north as Cabeus crater, located 5.5° from the pole but the northern traps extend out to 10° from the pole: listed in Table 3.1. This choice was to ensure a large enough set of the trapping regions, that had radii on the same order of magnitude from Moores' work, were taken into account. Selection of PSRs were restricted to the investigator's ability to confidently select the highlighted PSRs from Fig 3.1.2. This process required the identification of centres and the generation of circular approximations around the area. Necessarily, the resolution of the image, 100m/pixel LRO data, provides the lower limit for the size of the selected PSRs.

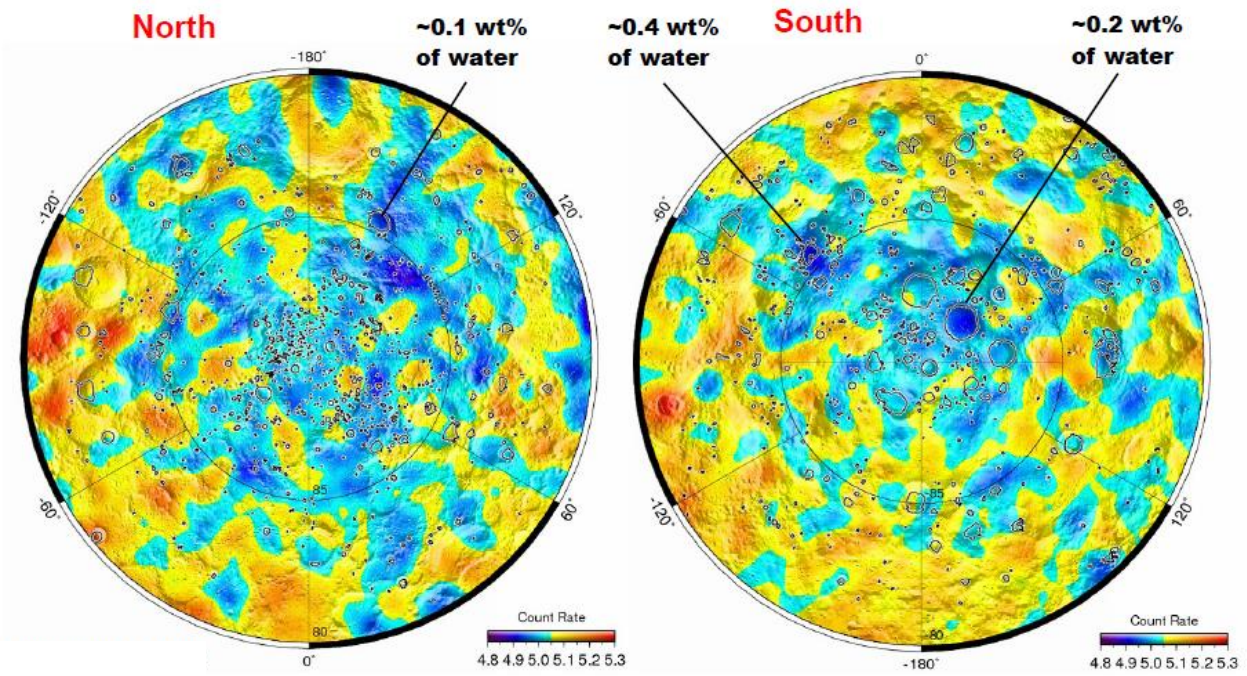

Figure 3.1.1: Neutron count rate of the lunar poles. Black features are part of the lunar relief map created by LOLA.

As seen in Fig 3.1.1, the largest water concentration in the polar regions resides within the south pole's northernmost large PSR, Cabeus crater. By choosing to consider traps up to 10° from the north pole this work can test the notion that, in Moores, 2016, Cabeus trapped the most because it was the furthest from the pole. Only the largest of the northern PSRs highlighted in McGovern, et al., 2013 were included in the code; those chosen are shown in Figure 3.1.2 and listed in Table 3.1. Though PSRs can be found closer to the equator, they are typically much smaller and are not taken into consideration for this work as the majority of PSRs lay near the poles [McGovern, et al., 2013]. In these warmer regions, particles will have much more energy to jump past PSRs, which are already miniscule compared to the surrounding area: less than 1% of the lunar surface lies in permanent shadow [McGovern, et al., 2013].

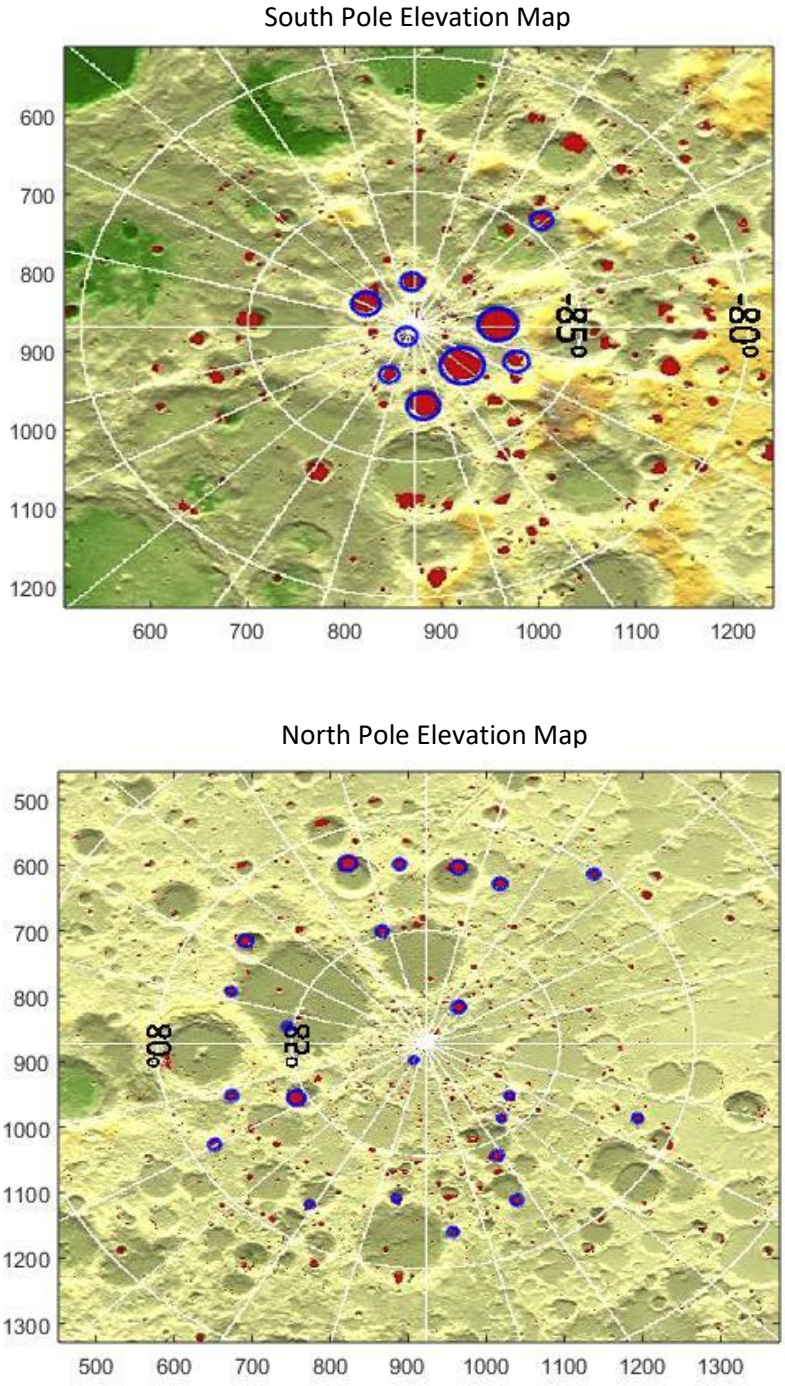

Figure 3.1.2: The axes of the grid are in pixel values. Background images retrieved from McGovern, et al., 2013. Red areas represent PSRs. Those encircled in blue are PSRs manually chosen for this work. South pole PSRs identical to those from Moores, 2016 (top). For the North pole (bottom), all selected PSRs reside north of -80° latitude as those closer to the equator become increasingly small and less significant.

Table 3.1: The latitude and longitude of the centres of each northern hemisphere PSR, followed by the diameter.

Latitude	*Longitude*	*Diameter [km]*	*Latitude*	*Longitude*	*Diameter [km]*
84.6	153	10	82.2	64	7
89.1	120	5	84.3	62	7
88.0	308	8	81.4	23	6
86.1	37	5	80.2	310	7
85.6	50	5	82.4	292	8
84.8	188	6	82.1	279	9
82.4	162	7	82.0	263	7
80.9	150	7	81.5	250	10
81.6	121	5	81.9	214	8
83.0	99	5	82.4	198	6
81.5	83	6	84.8	252	7

3.2 Ballistic Transportation

Due to the Moon being in the ecliptic plane for its entire orbit it is expected that small body collisions and solar wind implantation can occur at higher latitudes. Asteroid and comet impacts would necessarily come in at oblique angles but the craters we see near the lunar poles are proof they are possible. Prior to this work, initial positions were restricted to be on the equator at noon in the case of Moores, 2016 and ±40° latitude for Schorghofer, 2014. For this work particles are produced and given initial positions from a uniform random distribution when choosing longitude and latitude. In order to compensate for the fact that area between lines of latitude decrease, moving away from the equator, an arccosine function has been implemented. This production scheme will also remove any bias for traps that are near the production zone. Each particle is assumed to be a single H_2O molecule acting as tracers for larger sources. The water particles are assumed to have the same temperature as the regolith below it. The thermal heat of the regolith provides the energy needed for particles to hop along the lunar surface. For the simulations described in this work, each particle is traced over a period of 12 synodic months, where one synodic month is the time between one new moon and the next (29.53 days) and will henceforth be referred to as a lunation. The algorithm takes into account the position of the Sun in the sky and the particle's geographical location to determine the surface temperature at the particle's position. The surface temperature is then used to scale the particle's velocity, which is represented by a vector generated using a combination of Gaussian probability distributions, as detailed in section 3.3, an example of one is shown in Fig 3.2.1.

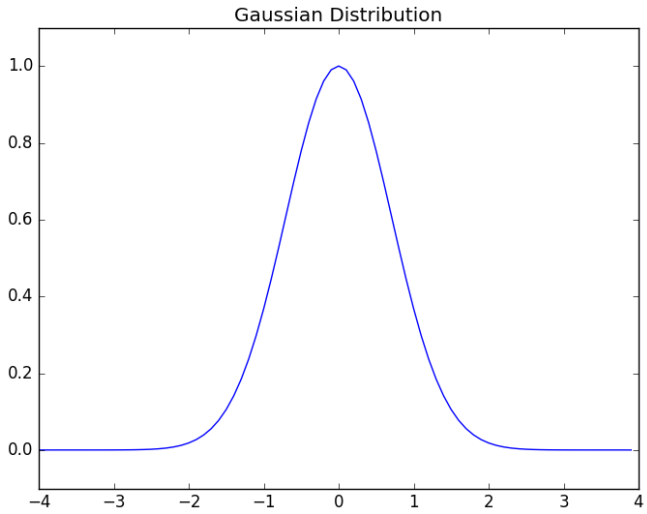

Figure 3.2.1: A Gaussian distribution with a median value of 0 ($\mu = 0$), and a standard deviation of 1 ($\sigma = 1$).The probability of selecting values further and further from zero becomes increasingly less likely (32% past 1σ, 5% past 2σ, 0.3% past 3σ). Velocities are generated by selecting value from the above Gaussian distribution, and then multiplied by Equation (5).

Residence time, τ, which represents the length of time a particle will be stuck to a surface, can be calculated using the simple relationship:

$$\tau = \frac{\theta}{E} \tag{2}$$

where $\theta = {\rho}/{m}^{2/3}$ is the adsorbate density of ice molecules, a function of density (ρ) and mass (m), and E is the sublimation rate, measured in molecules per cm^2 per second (Schorghofer and Taylor, 2007). Areal density is the number of particles found on the surface of a substance per unit area.

$$E = \alpha \frac{P_v}{\sqrt{2\pi k_b T_{surf} m_w}} \tag{3}$$

with the condensation coefficient $\alpha = 1$, the Boltzmann constant k_b =1.38065 × 10^{-23} m^2 kg s^{-2} K^{-1}, and $m_w = 18.015$ amu, the mass of H_2O. T_{surf} is the surface temperature which will vary based on time of day and location on the Moon's surface. Finally, P_v is the temperature dependent vapor pressure, which is described by:

$$P_v = P_{tp} \exp\left[\frac{-H}{R}\left(\frac{1}{T_{surf}} - \frac{1}{T_{tp}}\right)\right] \quad (4)$$

Vapor pressure also considers the triple point pressure of water, $P_{tp} = 611$ Pa, the sublimation enthalpy, $H = 51058$ J mol^{-1}, the gas constant, $R = 8.314$ J K^{-1} mol^{-1}, and the triple point temperature of water, $T_{tp} = 273.16\ K$. If one is to assume the regolith is extremely dry, H_2O will strongly bond to the particulate, thus raising the energy needed to sublimate off of the surface [Hodges, 2002]. To account for any particulate mixed with the ice, residence time is taken to be on the Moon's surface for 400 times longer compared to pure ice as suggested by Schorghofer, 2014.

3.3 Possible Outcomes

If a particle sublimates off of a surface it will inherit a velocity-vector, *v*, in 3D space. The distribution of speeds for a gas at a certain temperature are governed by the Maxwell-Boltzmann distribution. The Maxwell-Boltzmann distribution is created by the summation of three individual velocities for each direction, $\hat{x}, \hat{y}, \hat{z}$, from a Gaussian distribution:

$$P(v) = \sqrt{\frac{T_{surf}R}{m}}\, e^{-v^2} \quad (5)$$

Velocities in the z-direction are restricted to being positive to avoid trajectories going under the surface. As an example, Figure 3.3.1 shows the distribution of speeds generated for a surface temperature of 200 K:

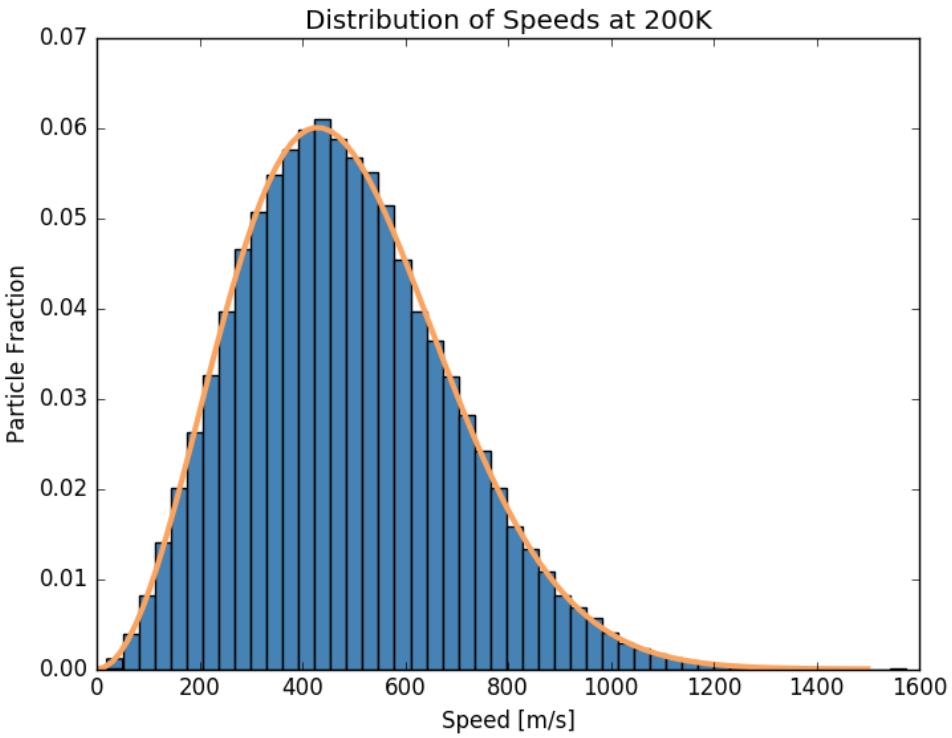

Figure 3.3.1: The distribution of 100,000 particle speeds generated by sampling Gaussian distributions for each of the particle's three degrees of freedom. The orange line is the analytic Maxwell-Boltzmann distribution. Refer to Appendix A.1 for the code.

For particles with relatively low speeds, to cut down on computational cost, the code will use uniform gravity for the simulation. Using $g = 1.62$ m/s^2 on the surface of the Moon and the initial velocity of the particle, it is elementary to find the flight time and distance, which is then converted into a change in longitude and latitude.

$$0.4\ v_{esc} = 0.4\sqrt{2GM/r}$$

$$= 0.4\ (2380)$$

$$= 952\ \text{m/s}$$

For speeds that are greater than 40% escape velocity, $v > 952$ m/s, particle hop distances are comparable to the Moon's radius and thus the code uses a non-uniform gravity to simulate its trajectory. Non-uniform gravity no longer assumes $g = 1.62\ m/s^2$, instead gravity is once again a function of radial distance from the center of the Moon. Equations are derived by Schorghofer and Taylor, 2007 from Kegerreis, et al., 2017. For any particle moving faster than escape velocity, the particle is assumed lost.

$$v = \sqrt{\sum {v_i}^2}$$

$$v = \sqrt{3}\,|v|$$

$$v = \alpha\sqrt{\frac{3\,T_{surf}R}{m}}$$

The variable α is a random variate selected from the Gaussian distribution which will typically range from -1 to 1. Using the above calculations and assuming α = 1, the typical surface temperature needed for a particle to escape is 654 K suggesting particle escape is rare due to the low temperatures on the Moon [Watson, Murray, and Brown, 1961b]. Particles may also be lost to photodissociation. The photodissociation of a water molecule is set to take place at a rate of $1.26\ x\ 10^{-5}$ molecules per second [Crovisier, 1989]. To decide whether a particle undergoes

photodissociation, a random number is generated from a uniform probability density and compared to the flight time divided by the photodissociation rate. This method ensures that particles with longer flight times are more likely to dissociate while still retaining the random nature of this process. Particles are designated a certain status allowing the code to differentiate those that are still in flight, have temporarily sublimated on the surface, experienced photodissociation, escaped the Moon's gravitational pull or been trapped in one of the PSRs. Those that have escaped, photodissociated, or been trapped are reset to a random location on the surface after the tally for its respective end result has been increased. This allows the code to actively produce new particles from particles that are no longer moving or have escaped the system, thus saving memory.

3.4 Temperature Profile

The temperature profile is derived by creating a three-dimensional grid defined by longitude, latitude and depth beneath the surface. The surface is estimated by a 360-by-89 grid of points, 360 columns representing each line of longitude and 89 rows representing all even lines of latitude, with two additional points outside of the grid for the north and south poles. This method allows for the calculation of temperature at the cross section of every even numbered line of latitude with all lines of longitude. The third dimension of the grid, depth, extends 1000 points below the surface and tracks the diffusion of heat from the Sun below the surface. Heat diffusion is calculated by implementing the Crank-Nicolson method to the one-dimensional heat equation [Crank and Nicolson, 1996]:

$$\frac{\delta}{\delta t}u(x,t) = \frac{k}{\rho c_p}\frac{\delta^2}{\delta x^2}u(x,t) \qquad (6)$$

where we solve for the temperature, $u(x,t)$ by using the thermal conductivity $k = 2.5 \times 10^{-3}$ W m^{-1} K^{-1}, and the volumetric heat capacity, $\rho c_p = 10^6$ J m^{-3} K^{-1} [Schorghofer, 2014].

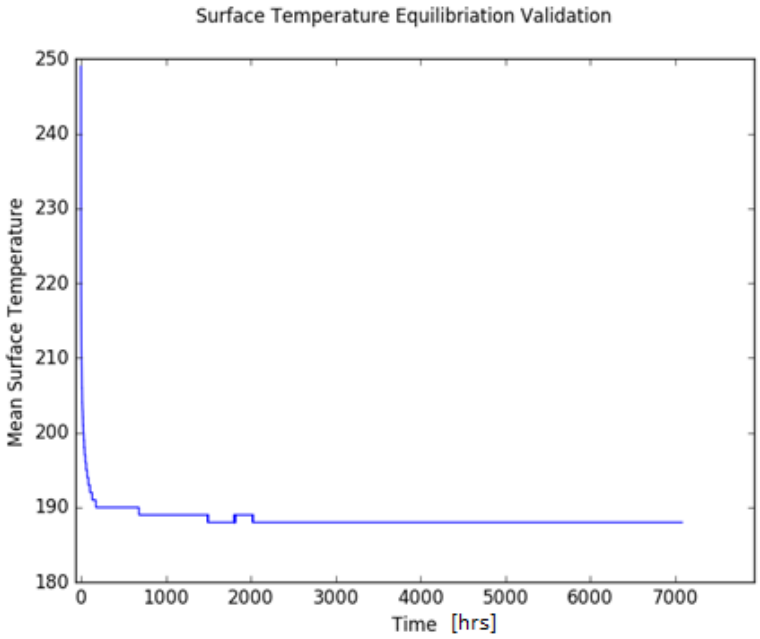

Figure 3.4.1: The mean lunar surface temperature over 10 lunations. The flat line shows the surface has equilibrated.

The lunar regolith bond albedo, the fraction of incident light that is scattered back into space, over all wavelengths and phase angles, is set as 0.11, as recommended by Schorghofer, 2014, this means only 89% of the Sun's radiation is being absorbed and heating the ground. For simplicity, the Moon's inclination angle has been assumed to be zero, rotation period is taken to be the average lunation and orbital distance is restricted to 1 AU. Due to the heat equation's dependence on time, the program is set to run for 10 lunations before introducing particles to the system. Every point on the surface is initially set to 250 K and Figure 3.4.1 shows how the mean

surface temperature has settled at 190 K which is not expected to undergo anymore drastic fluctuations. Furthermore, the resultant temperature profile is compared to data presented by Vasavada et al., 2012 in Figure 3.4.2, so, one can proceed with particle simulations knowing the surface temperature is representative of the lunar surface.

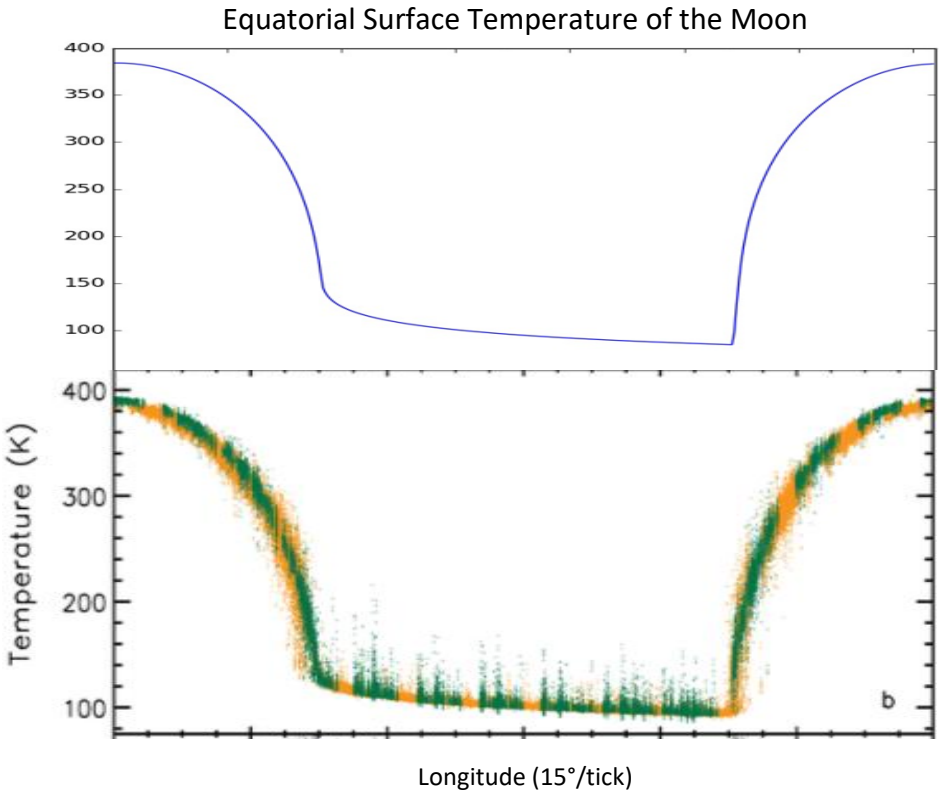

Figure 3.4.2: The equatorial surface temperature found by this work (top) juxtaposed to Diviner observations (bottom) [Vasavada et al., 2012]. This comparison allows us to continue with simulating particles on the lunar surface with confidence.

3.5 Particle Simulation

Once a temperature profile was successfully generated simulations of the ballistic transport of water particles were conducted. An initial population of 20,000 particles, which were placed randomly on the lunar surface, were given 12 lunations to move around on the surface. Note that more than 20,000 particles were simulated due to the production function, detailed in A.1, which allowed for any trapped, escaped or photodissociated particles to be recorded and then reinstated as a 'new' particle with a random location. The code has been designed to advance all particles and update the lunar temperature profile in one-hour increments. The process was simulated 12 times and then each trapping area was individually averaged across all runs to ensure the results were statistically robust. To account for any error in the mean concentrations of PSRs, 95% confidence intervals (CI) were calculated using the following formula:

$$95\%\ CI = 1.96\frac{\sigma}{\sqrt{n}} \tag{7}$$

where σ is the standard deviation and n is the number of runs.

Chapter 4

H_2O Simulation

4.1 Results

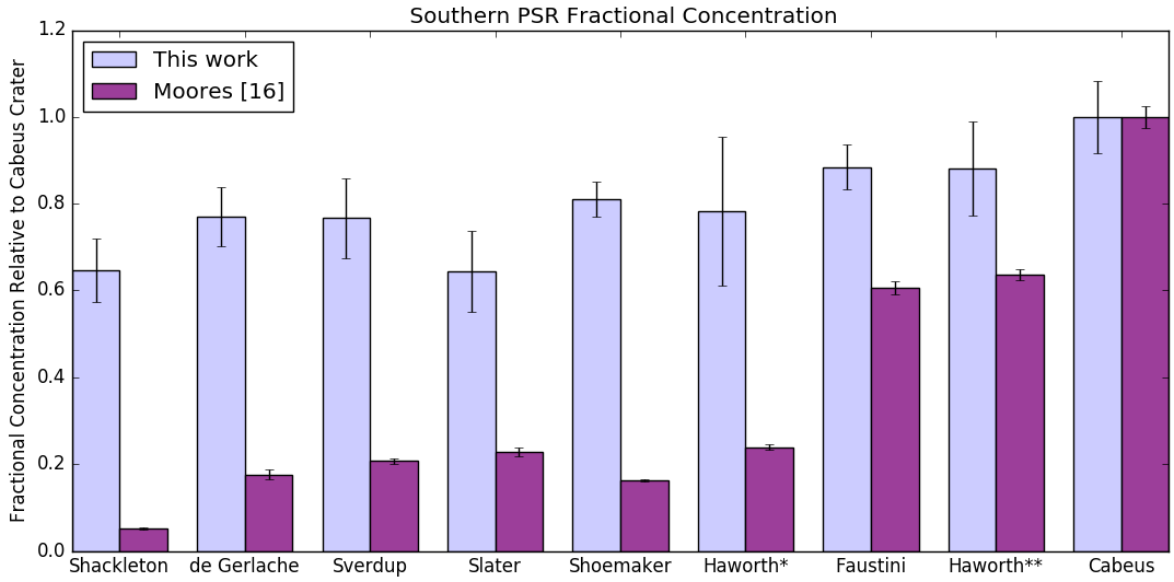

Figure 4.1.1a: Concentration of water particles compared to Cabeus crater, organized with craters furthest from the south pole on the right. The light purple are results found by this work, the dark is those found by Moores [2016]. *Haworth Crater **Haworth Lowlands

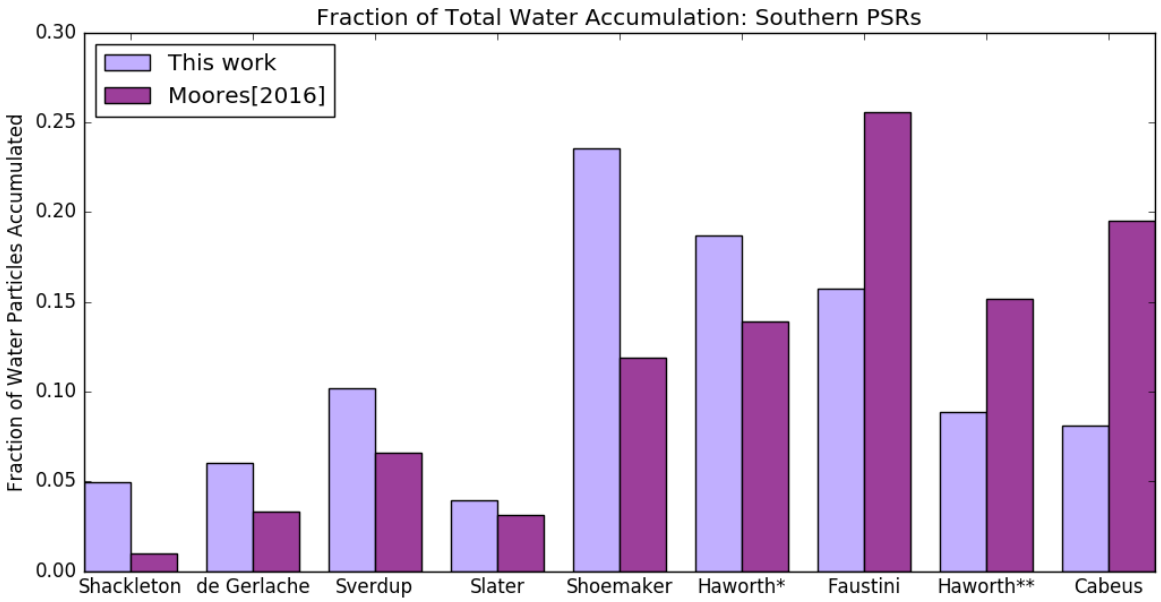

Figure 4.1.1b: Fraction of total water trapped accumulated by each PSR in the southern hemisphere. Note, unlike the fractional concentration from Figure 4.1.1a, fraction accumulated values do not take the area of individual PSRs into account. Values from this work are compared to those of Moores [2016].

After completing all simulations, the total number of particles simulated and captured are an order of magnitude less than those from Moores [2016]: seen Figure 4.1.1b. The number of particles captured is large enough that these errors do not dominate the data despite the error bars being significantly larger than those of Moores [2016].

The work of Moores, 2016 suggests that the current distribution of water ice was due to a diffusive barrier created by south polar PSRs. In other words, traps closer to the poles would capture fewer particles per square metre due to particles being trapped and sequestered by the lower latitude traps. This work suggests that traps in the vicinity of one another do not play as important a role as previously suggested.

To gain a greater understanding of why this work's results differed from Moores [2016], one can point to three primary differences: the photodissociation algorithm, the particle spawn location and time, and the temperature profile generation. Firstly, Moores uses an Arrhenius equation when modelling the probability of photodissociation:

$$if: x < 1 - e^{-t/\tau} \tag{8}$$

This work uses a simple linear equation, which is the Taylor expansion of (8):

$$if: x < t/\tau \tag{9}$$

In the above equations x is a randomly generated number between 0 and 1, t is the flight time of the particle and τ is the photodissociation time. As t increases the probability of photodissociation increases, and in this work's case, once $t \geq \tau$ the particle is guaranteed to photodissociate. Secondly, Moores only spawns molecules at noon on the equator, the subsolar point, versus this work which allows particles to spawn anywhere on the surface of the Moon. Thirdly, this work calculates the surface temperature for each individual point on the grid independently versus Moores' less time intensive scaling relation as stated in equation (5). In order to understand how these aspects will affect the trapping efficiencies of PSRs, the sections of code mentioned above will be altered, independently, to resemble the work previously done by Moores.

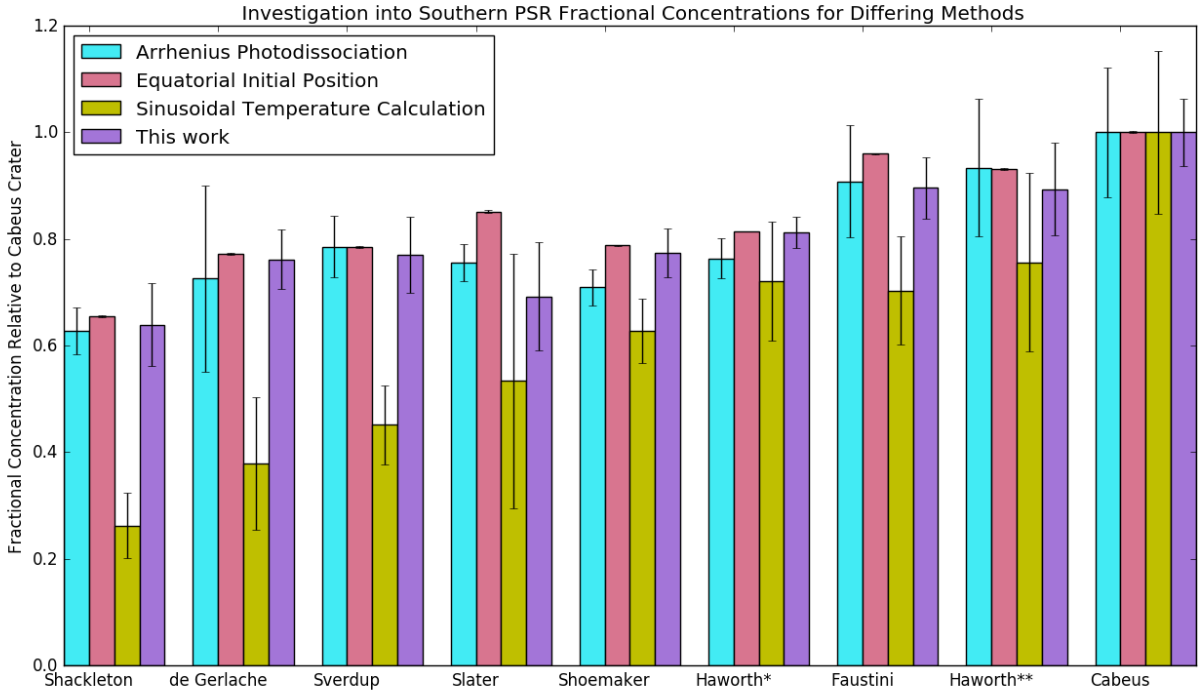

Figure 4.1.2: Fractional concentrations of each of the south polar PSRs using different methods. Purple: This work, identical to the values in Figure 4.1.1a Yellow: Replacing the temperature profile with the sinusoidal equator temperature relation from Moores [2016]: Equation (5). Red: Spawning all particles on the equator with the Sun highest in the sky (the sub solar point). Cyan: Replacing the linear photodissociation rate with equation (8).

The changes to photodissociation rate and equatorial spawning do not seem to have large effects on the diffusion of particles. It is important to note that the equatorial spawning data have much smaller error bars, similar to that of Moores' work, refer to Figure 4.1.1a. When spawning all particles at the sub solar point, the warmer regolith allows them to spend more time in flight versus those beginning their journeys in polar regions. Particles in polar regions spend more time frozen to the regolith and a particle can only photodissociate whilst in flight. This means that the code will be able to simulate more particles with Moores' scheme: leading to the smaller confidence intervals.

Most notably, the change in temperature calculations caused a decrease in ice concentration for the highest latitude PSRs. This seems to be the reason behind the conflicting values between this work and Moores [2016]. It can be said that the sinusoidal scaling of the equatorial surface temperature may not be optimal when simulating processes so close to the poles.

. In Figure 2.2.1, a plot from Moores, 2016, we can see particles typically exhibit hop distances ranging from 10^3-10^5 m, the diameters of the largest traps seen at the poles are 10^4 m and, from Figure 2.1.2, cover less than 10% of the total area in the region. Due to the fact that surface temperature is a major proponent in calculating hop distances, it is valuable to understand how particle hops differ in this work compared to Moores, 2016. In Figure 4.1.3, one can see that average hop distance does not vary, latitudinally, as much as suggested in Figure 2.2.1. Furthermore, by organizing hops by their size, Figure 4.1.4 shows the majority of hops are at least one order of magnitude larger than PSRs.

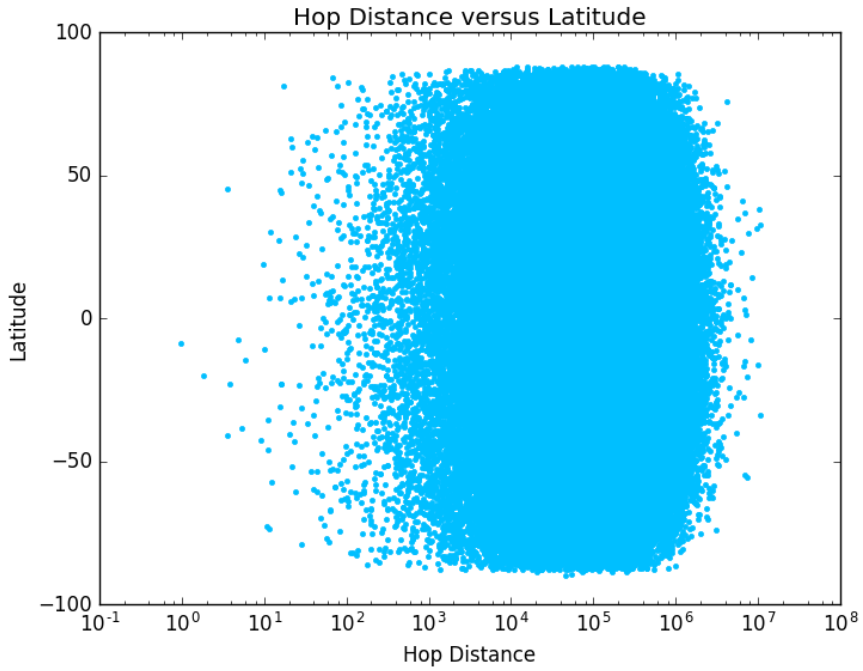

Figure 4.1.3: A plot generating by recording the hop distances over 1 lunation of particle simulations. There is a latitudinal dependence for hop distance but less so than suggested in Figure 2.2.1: from Moores 2016.

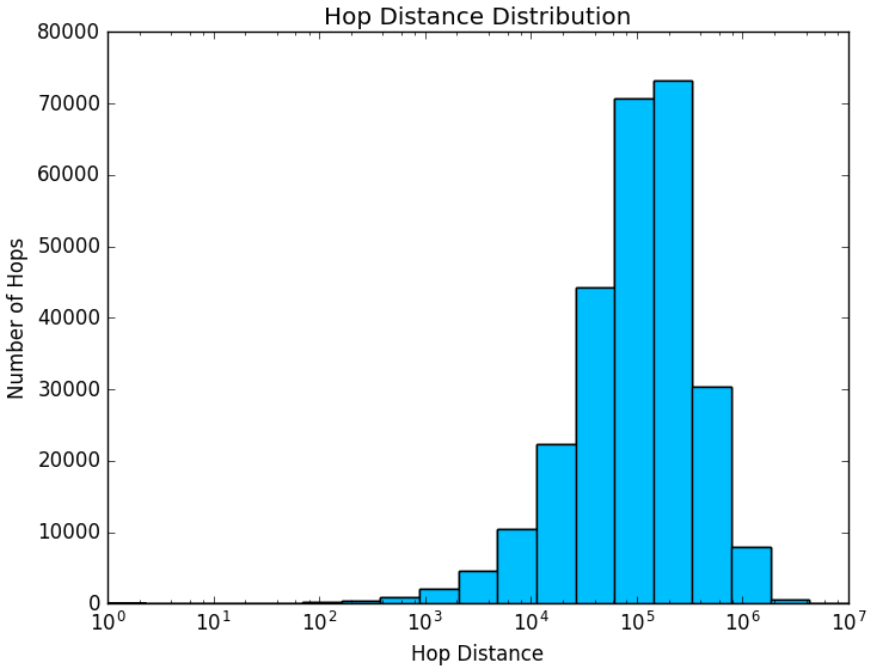

Figure 4.1.4: Distribution of hop distances after 1 lunation of simulations

According to Moores [2016], PSRs should act as physical barriers to particles travelling from low to high latitude regions. This work will create hypothetical trapping regions to test the validity of this statement Based on the fact that PSRs do not dominate the landscape, particles should more often than not hop unaffected by PSRs. This is not to say PSRs can not trap particles, rather that trapping is a low-probability, random process since $\frac{average\ hop\ distance}{trap\ diameter} \gg 1$. This makes it more likely that a diffusion pattern will be caused by the surface temperature rather than PSRs.

In order to test the theory that PSRs can act as physical barriers, a spherical cap, the area between the pole and a line of latitude, and a ring trap, defined by the area between two lines of latitudes, were placed at both poles: refer to Figure 4.1.5.

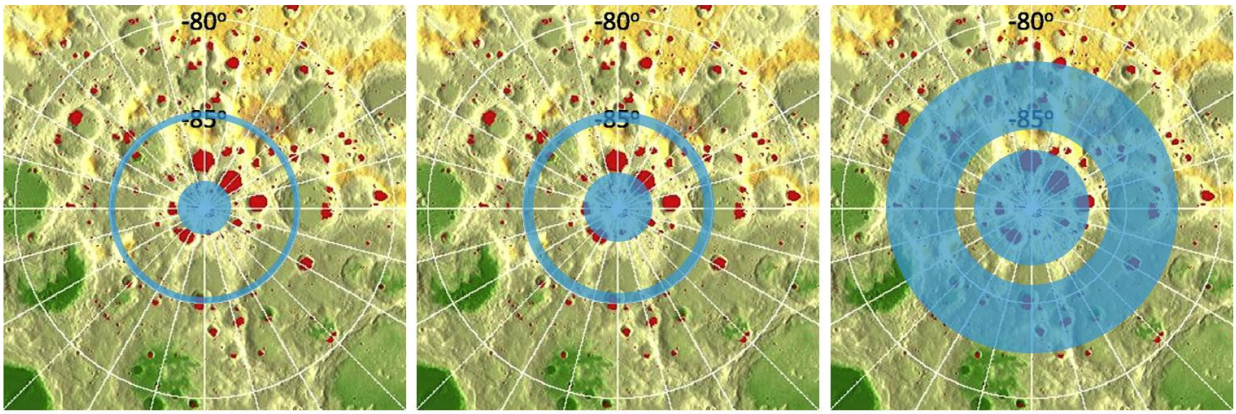

Figure 4.1.5: The three continuous ring and spherical cap trapping configurations for Cases 1-3. The blue areas are the traps shown with reference to the lunar south pole and its PSRs in red. Background image from McGovern

Table 4.1.1: Cap and ring trap simulations. The set ups were symmetric about the equator: a ring spanning the space between two lines of latitude and the caps defined as the area between a line of latitude and the pole.

Case	Cap Surface Area [km^2]	Ring Surface Area [km^2]	Volatile Fraction Captured by Spherical Cap
1	5000	5000	0.040
2	10000	10000	0.071
3	25980	95126	0.049

The surface area of 10 000 km^2 for Case 2 was chosen to give the ring a width of 10.3 km, which is on the same order of magnitude we typically see traps at this latitude. Cases 2 & 3 were created to test how trapping changed when the rings were thinner or thicker, respectively. From Case 1 to Case 2 one can see an increase in the volatiles reaching the spherical cap despite the increased thickness of the ring trap. Whereas there is a decrease in volatile capture when increasing both the ring and cap thicknesses from Case 2 to Case 3. With this information one can deduce that particle hop distances are too large for PSRs on the Moon to affect their diffusion pattern. Only in Case 3 where the ring traps span multiple degrees of latitude (86° – 83°), is there a significant affect on particles reaching high latitude regions.

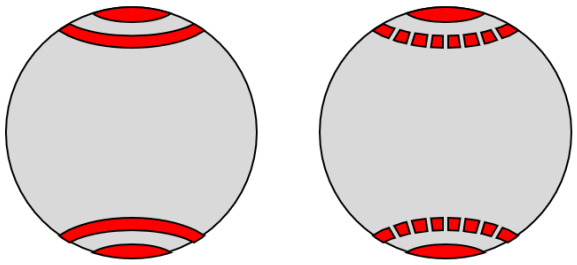

Figure 4.1.6: The continuous (left) and checkered (right) ring trap configurations as viewed from the equator. Red areas represent trapping areas. Trap areas compared to the surface area of the Moon are not to scale in this diagram.

In addition to the continuous rings, checkered ring traps were considered. In the following cases, instead of having the trap extend from 0°-360° longitude, the checkered rings would only trap particles that fell between 0°-1°, 2°-3°, 4°-5°, etc. cutting the trapping area in half.

Table 4.1.2: Cap and checkered ring trap simulations. The set ups were identical for both poles. A ring consisted of 180 sections each spanning the space between two lines of latitude. The sections were one degree of longitude wide and spaced one degree apart. The caps are defined as the area between a line of latitude and the pole.

Case	Cap Surface Area [km^2]	Ring Surface Area [km^2]	Ring Trap Pattern	Volatile Fraction Captured by Spherical Cap
1	5000	2500	Checkered	0.047
2	10000	5000	Checkered	0.082
3	25980	47563	Checkered	0.074

When changing the continuous ring to a checkered one, the ring captured fewer particles and the cap captured more, as expected, in all cases. When adding gaps to the rings, the rings overall trapping area decreased by 50%, despite this the caps only captured 17.5% more particles in Case 1 and 15.5% more in Case 2. Whereas in Case 3, where the ring trap is significantly thicker, the cap's capture rate increased by 51%. This experiment showed, once again, that it would take enormous traps, spanning multiple degrees of latitude, to create conditions that have a significant effect on volatile trapping in high latitude regions.

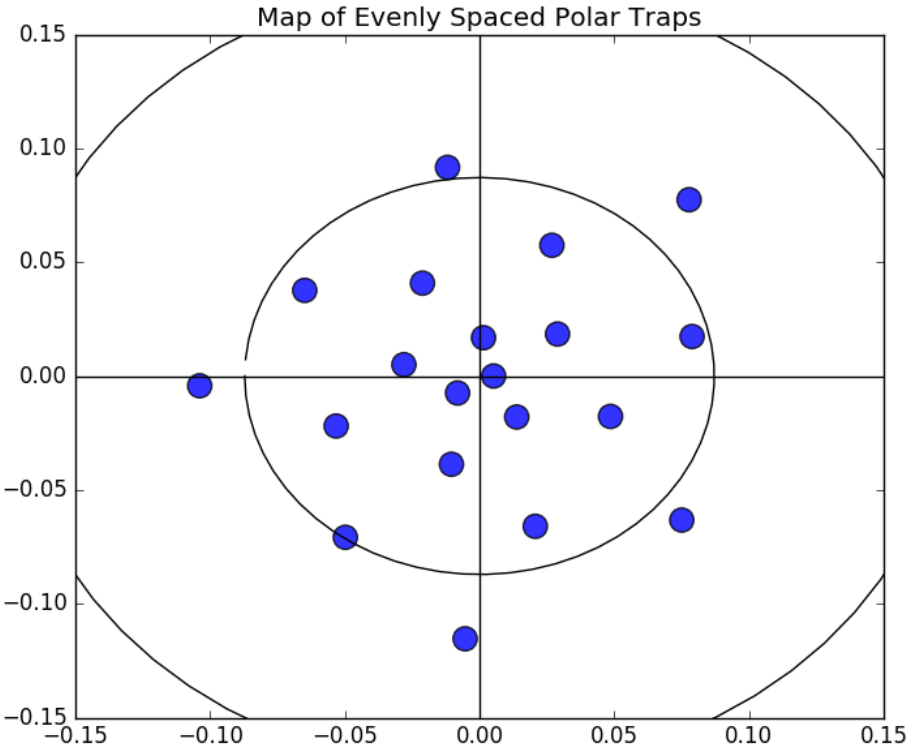

Figure 4.1.7: A plot showing the 20 traps, with 15 km diameters, centered around the south pole. The two concentric circles are 85° and 80° latitude.

Figure 4.1.7 consists of 20 traps, with 15 km diameters, spaced longitudinally by 0.33° and latitudinally by 0.618 revolution about the pole. This setup ensures the traps extend from 83°-89°, the area of interest for this work, and that there is space between traps: reducing inter-trap interactions. Figure 4.1.8 shows the results after averaging 6 runs of 12 lunations. The red line is a logarithmic fit of the data, as suggested for diffusion on a sphere by Coombs, et al., 2009. This will serve as a guide for fitting data in Figure 4.2.2.

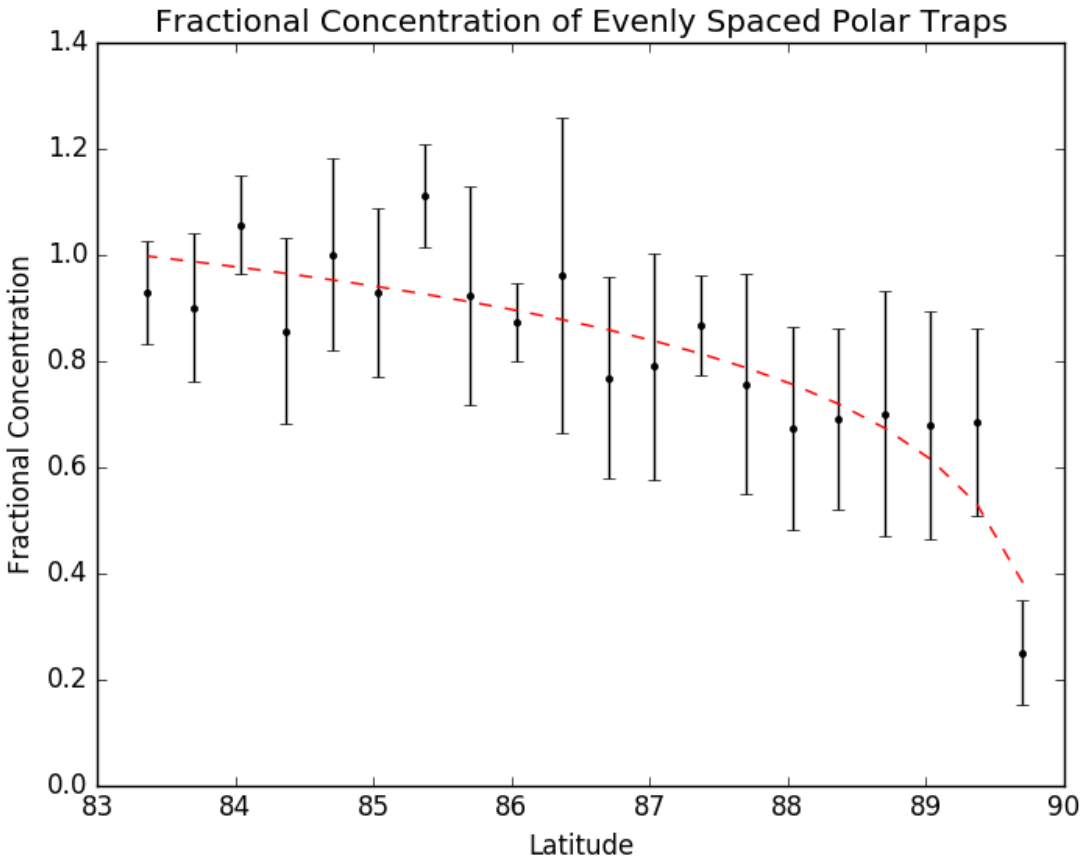

Figure 4.1.8: Fractional concentration of 15km diameter traps. Red dashed line is the logarithmic fit.

.

4.2 Discussion

Figure 4.1.1a looks at the fractional concentration, y-axis, of each of the south polar PSRs, x-axis, found by this work compared to Moores [2016]. This work's change in concentration of PSRs when moving closer to the pole, though present, is not as large as suggested by previous work. By comparing the fractional concentrations of Cabeus crater versus Shackleton according to Moores' results in Figure 4.1.1a, lower latitude traps are expected to be on the order of 10 times more concentrated with water ice. This is not apparent in the results from Figure 4.1.1a and only occurred in extreme cases in the ring and cap trapping configurations. Apart from Cabeus, the mean concentrations for each trap lay outside the standard deviation of the mean for either value, this work or Moores, 2016. This work's error bars are significantly bigger due to the difference of method. Moores, 2016 simulates particles to their completion one at a time, guaranteeing a set number of data points whereas this work does not. Instead an initial 20,000 particles are simultaneously simulated, when particles become trapped, photodissociate or escape, their fate is tallied, and a new particle is created with a random starting position. This method allows for a more realistic distribution of starting positions but requires a hard-coded end that necessarily leaves particles still in transit and unrecorded thus resulting in a smaller sample size. This diffusion phenomenon is more likely due to the particles' tendency to migrate away from the poles. Hop distance is governed by surface temperature; thus particles will make increasingly smaller jumps sublimating off of the surface near the poles. This imbalance of larger hops occurring further from the poles creates an unstable resting point at the Moon's poles.

The north pole has fewer overall PSRs for trapping to occur thus, to ensure a large enough sample was taken, the chosen PSRs extend down to 10° from the pole. This serves to challenge the notion that this model will tend to predict that low-latitude PSRs would trap more than the polar counterparts. From Figure 4.2.2, there are large clusters of low concentration PSRs on either side of 85°. Siegler, et al., 2016 proposed that the reason the highest concentrations of lunar surface ice were found approximately 5° from the poles was due to water ice trapped billions of years ago. The realignment of the Moon's axis of rotation, due to changes in the inertia tensor, could exhibit shifts up to 15° from the original locations. Siegler, et al., 2016 credits this shift as the major player in the water ice concentrations we see on the lunar surface. This theory relies on the assumption that any volatile infall, since the realignment, is inconsequential compared to previously deposited ice. With this work we see there is decrease in trapping efficiency in the polar extremes (87°-90°). According to the logarithmic fit, trapping efficiency would increase near the equator which is not what is observed on the Moon. According to Figure 2.1.2, PSRs decrease in size in low-latitude regions and fall to less than 1% area coverage at 78°. The fact that there is almost no area to capture particles explains why the majority of trapped and sequestered ice is found in a 'Goldilocks Zone', where there are available PSRs and the mean passage time is smallest [Moores, 2016].

From any randomly distributed initial population, this work predicted that 5.3% ± 0.1 to be trapped and sequestered within PSRs. As previously discussed, this method stops simulating before a large population of particles are trapped or destroyed. Spawning particles in polar regions cause them to spend more time frozen to the surface instead of ballistically travelling, unlike their equatorial counterparts.

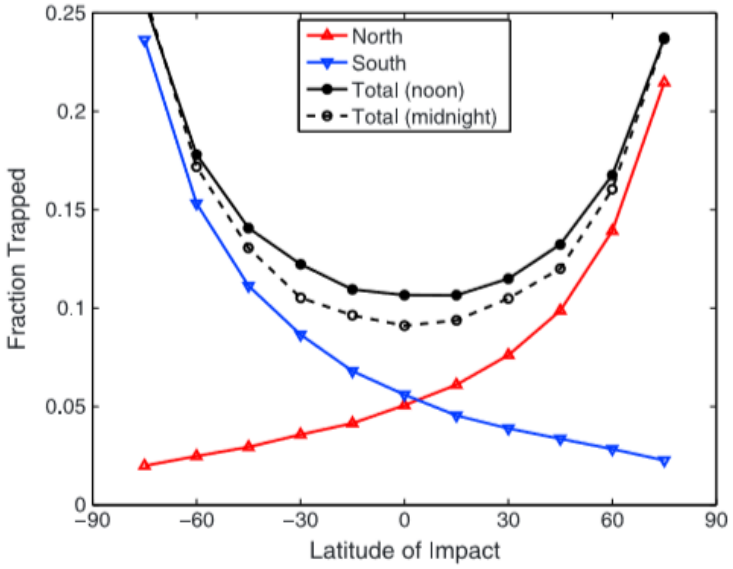

Figure 4.2.1: Fraction of water trapped in the north and south polar regions as a function of the latitude of the source [Schorghofer, 2014].

According to Figure 4.2.1, retrieved from Schorghofer 2014, trapping efficiency of PSRs will increase as distance to the source decreases. Following this logic, if the particles on polar, non-PSRs were simulated further they would increase the overall trapping percentage of PSRs. Considering incoming water sources (solar wind implantation, asteroid and comet impacts) can be estimated to be on the order of $10^{13} – 10^{14}$ kg over 1 billion years [Ong, et al., 2010][Arnold, 1979], one can expect the process of ballistic transport to account for 10^{11} kg of ice near the poles, as a conservative estimate.

This work's results support the theory that active water deposition on the lunar surface can yield the patterns we see now. This work has shown that one can find global maxima, in terms of trapped volatiles, at latitudes in accordance with observational results. One can also see the similarity in concentration of Cabeus and Siegler's northern "paleo-pole" [Siegler, et al., 2016]. Yet in contrast to Siegler, et al., 2016, there is no longitudinal bias in regard to trapping. In Figure

4.2.3, there is no apparent trend suggesting PSRs of similar longitudes would exhibit different trapping efficiencies. The code has achieved this by means of simple ballistic simulations without taking into account any changes in the inertia tensor or previous depositions.

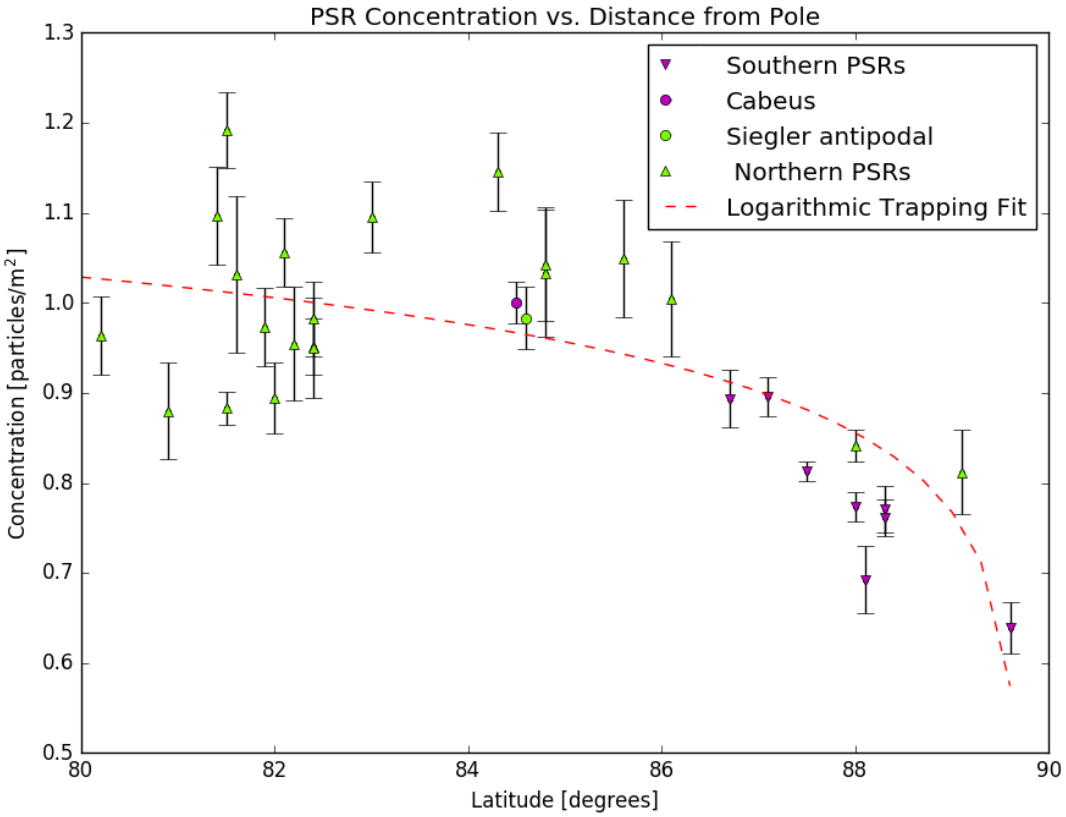

Figure 4.2.2: Absolute latitude versus concentration normalized to the value found at Cabeus crater. Notice how concentrations rise as distance from the poles increase and there is a cluster of low concentration points at 82°.

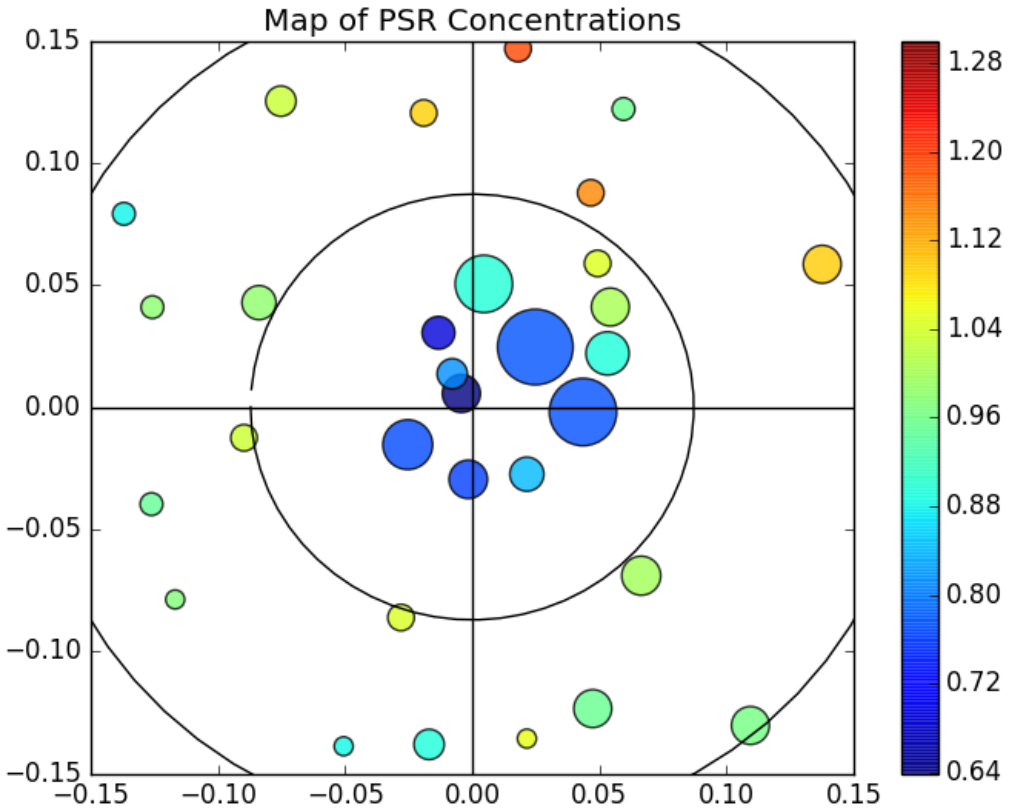

Figure 4.2.3: Concentration map of both north and south poles, superimposed. Note that traps at similar distances from the poles exhibit similar concentrations.

Chapter 5

Volatile Species Comparison

5.1 Introduction

Previous work has largely focused on the migration of water molecules over the lunar surface [Siegler, et al., 2016][Moores, 2016][Butler, 1997][Schorghofer, 2014]. Clearly this is of interest because of our reliance on water to survive on Earth, as well as life support for any long-term interplanetary missions or fuel production. The migration patterns of other volatile species have yet to be modelled. Other abundant volatiles are expected to be seen in space include simple hydrated compounds; ammonia (NH_3), methane (CH_4), and hydrogen sulfide (H_2S) or compounds made of elements created by fusion in stars; carbon dioxide (CO_2). These simulations can potentially constrain the source of these volatiles on the lunar surface. By simulating multiple different species and comparing the results we can work backward from the results to find the volatile concentrations of the average volatile source.

5.2 Implementation

With a method similar to that of water ice, described in Chapter 3, simulations of the trapping efficiency patterns of five other volatiles found in the LCROSS ejecta plume were conducted: hydrogen sulfide, ammonia, ethene, carbon dioxide and methanol. Table 5.1 breaks down the four main physical attributes governing the ballistic behaviors of these volatiles:

Sublimation Enthalpy:	The energy needed for a molecule to sublimate off of the surface of the Moon
Mass:	Mass of one molecule of substance
Photodissociation Rate:	The number of molecules expected to photodissociate per second during ballistic motion
Density:	Used for calculating the residence times for volatiles as stated in Section 3.2

The enthalpy values used for this work represent the energy needed for a volatile to sublimate off of other volatiles, whereas in most cases volatiles are adsorbed to lunar regolith. Adsorption enthalpy values can vary by orders of magnitude and are not well constrained at the time of this work, this sublimation enthalpies will be used in their place.

As before, the temperature profile was equilibrated, and runs were carried out with an initial 20,000 particles, where the algorithm permitted the particles to respawn after they were either destroyed or trapped. The constants governing the ballistic behaviour for each species are provided in Table 5.1: these values were entered into the code to simulate the appropriate volatile.

This work will only look to compare the trapping efficiency of Cabeus crater, for it is the only crater for which observational data have been collected at the time of writing. Here, we define the trapping efficiency to be the average number of particles trapped in Cabeus compared to overall particles simulated, or:

$$\text{trapping efficiency} = \frac{\text{particles trapped by Cabeus}}{\text{total particles simulated}} \tag{8}$$

Normalizing LCROSS's observed volatile concentrations by the percentage of trapped particles, per species type, will yield the projected composition of the initial impactor.

Table 5.1: Sublimation enthalpy, mass, photodissociation time and density of simulated volatiles. The sublimation threshold is the temperature at which the species sublimates at a rate of 1 molecule/s·m^2. References: **a.** Crovisier, 1989. **b.** Schorghofer et al., 2016. **c.** Clark, Cockett, Eisner, 1951. **d.** Everstreet, Giauque, 1937. **e.** Tickner, Lossing, 1951. **f.** Giauque, Egan, 1937.

Species	H_{sub} [kJ]	Mass [amu]	τ_{dis} [a] [10^{-6} mol/s]	Density [g/cm^3]	Sublimation Threshold [K]
H_2O	51.06 [b]	18.01	12.6	0.917	75.3
H_2S	22.5 [c]	34.08	320	1.36	39.3
NH_3	31.2 [d]	17.03	184	0.817	51.4
C_2H_4	18.4 [e]	28.05	48	1.18	32.9
CO_2	25.2 [f]	44.01	2	1.5	43.3
CH_3OH	41.4	32.05	12	0.792	64.6

5.3 Results

After 6 runs per species, the number of trapped particles tended to converge and thus Figure 5.3.1 could be produced with confidence. Each column represents the average fraction of particles captured by Cabeus crater for each volatile species. Points of note are the extremely low values of H_2S and NH_3 that were captured by Cabeus, in relation to the other volatile species.

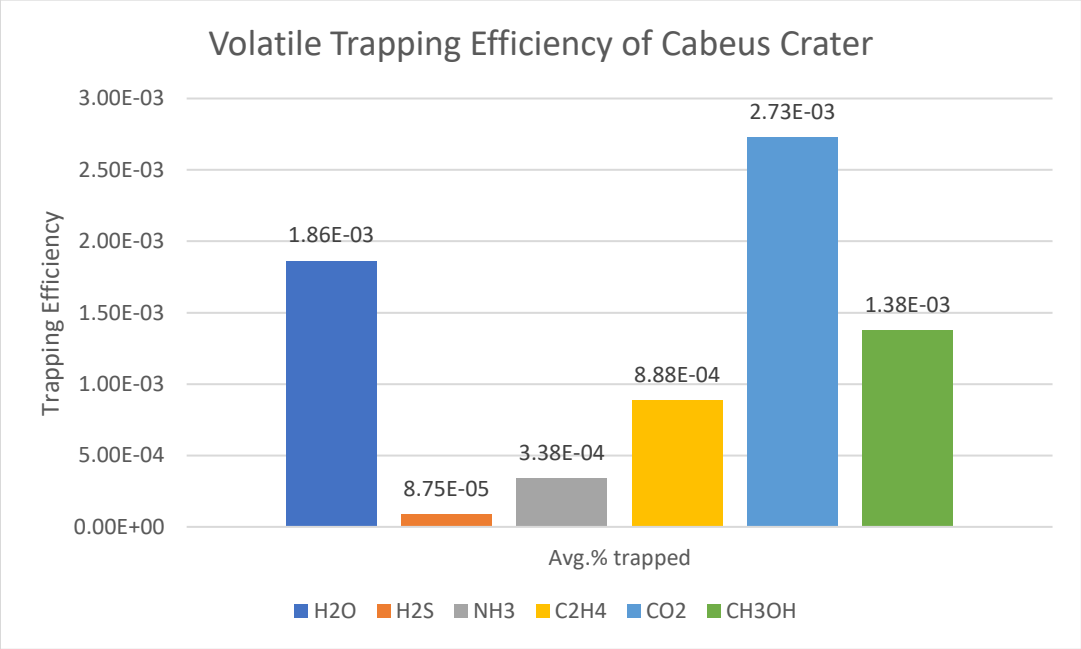

Figure 5.3.1: Average trapping efficiency of each volatile species simulated. Values shown are the average fraction of particles trapped by Cabeus crater.

In order to understand why H_2S is almost two orders of magnitude less efficient at being captured by PSRs each of the four physical attributes, listed in Table 5.1, was investigated. To do this, particles were simulated assuming they were identical to water except for one of the four attributes which was replaced with the H_2S value. In Figure 5.3.2, the green area represents the

values which fall within one standard deviation of the trapping efficiency of water, ± 4.25 (10^{-4}). A change in the dissociation time is the only attribute that creates a significant difference in trapping efficiency.

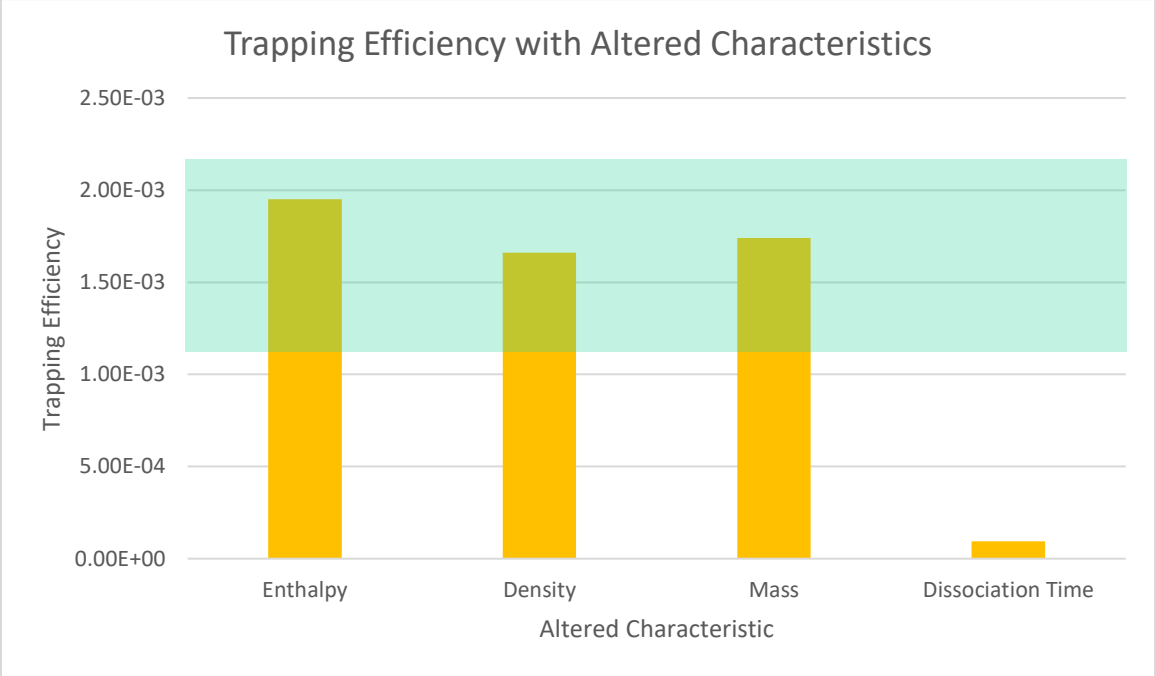

Figure 5.3.2: Trapping efficiency experiment based on changing a single characteristic of water to that of hydrogen sulfide. Each column represents the trapping efficiency of Cabeus crater after changing the characteristic below the column from Table 6.1. The green area represents the values that fall within one standard deviation of the trapping efficiency of water.

Figure 5.3.3 shows the relative abundances of the various volatile species found within Cabeus Crater from the LCROSS impact experiment (left) juxtaposed with the simulated source concentrations from our model. The plot on the right was created by dividing the volatile ratios found at Cabeus, Figure 5.3.3 (left), by their respective trapping efficiencies, Figure 5.3.1. This process should help us predict the initial amount of a volatile needed in order to produce the ratios found in Cabeus: low trapping efficiencies lead to higher initial concentration and vice versa. As

can be seen here, the modeled results of the source ratio differ substantially from the measurements of LCROSS. These results are unexpected as the composition of the impactor inferred from our work is atypical, as most smaller source bodies (comets and asteroids) are dominated by water ice [Despois, et al., 2006][Campins, et al., 2010][Rivkin and Emery, 2010].

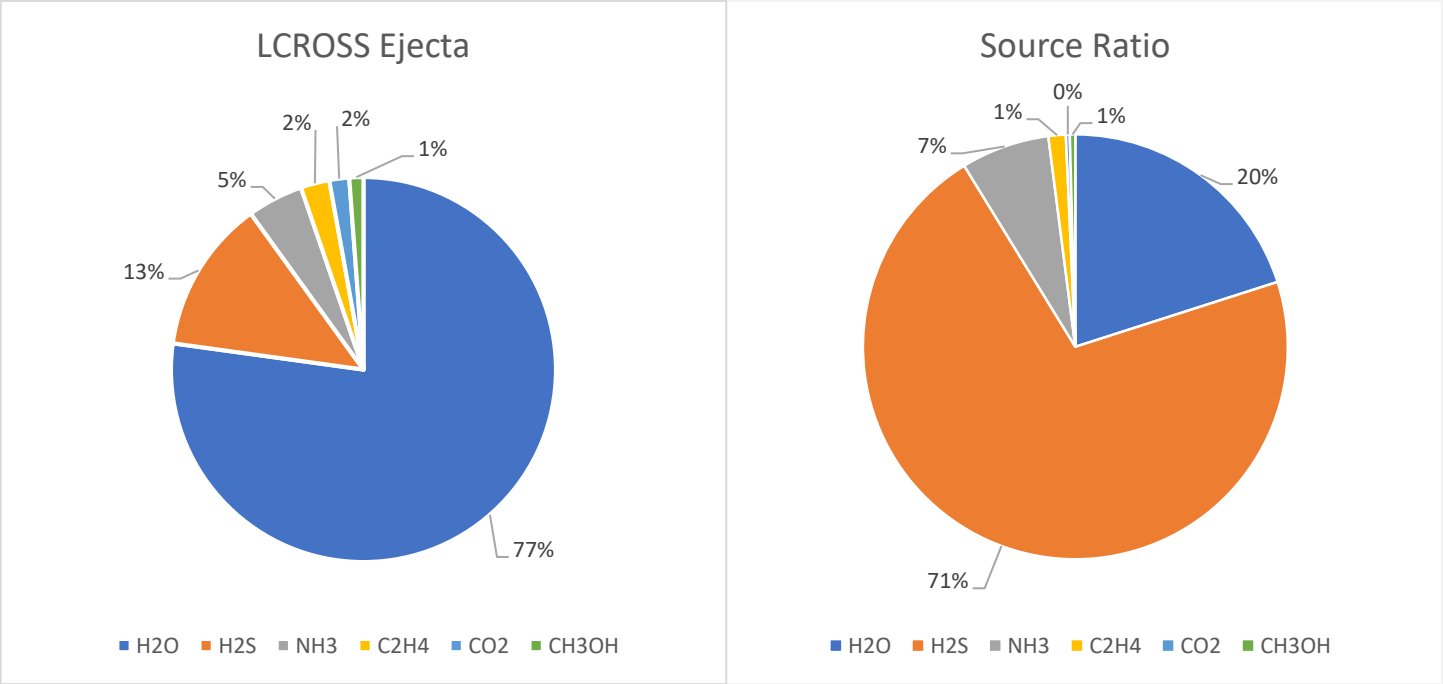

Figure 5.3.3: Composition of Cabeus from LCROSS impact ejecta (left) and the predicted source ratio from this work (right).

5.4 Discussion

The cold temperatures of PSRs do not contain enough thermal energy for water ice to sublimate and escape the traps, however, this fact can not be assumed for all volatiles species. Table 5.4 are the calculated residence times at 50 K, a typical value for lunar PSRs, for the other

volatile species: refer to Appendix A.1. These results show that all species are expected to remain adsorbed to the surface regolith for extended periods of time, thus will be assumed trapped indefinitely. Furthermore, Figure 5.4.1 shows the sublimation rates for all considered volatile species. In the zoomed plot (right), the red dashed line identifies the temperatures in which volatile sublimation rates decrease to less than 1 molecule per metre squared per second. The least volatile, H_2O, passes this threshold at 75 K and the most volatile, C_2H_4, passes at 32 K both of which lie within the expected range of temperatures for lunar PSRs [Paige, et al., 2010].

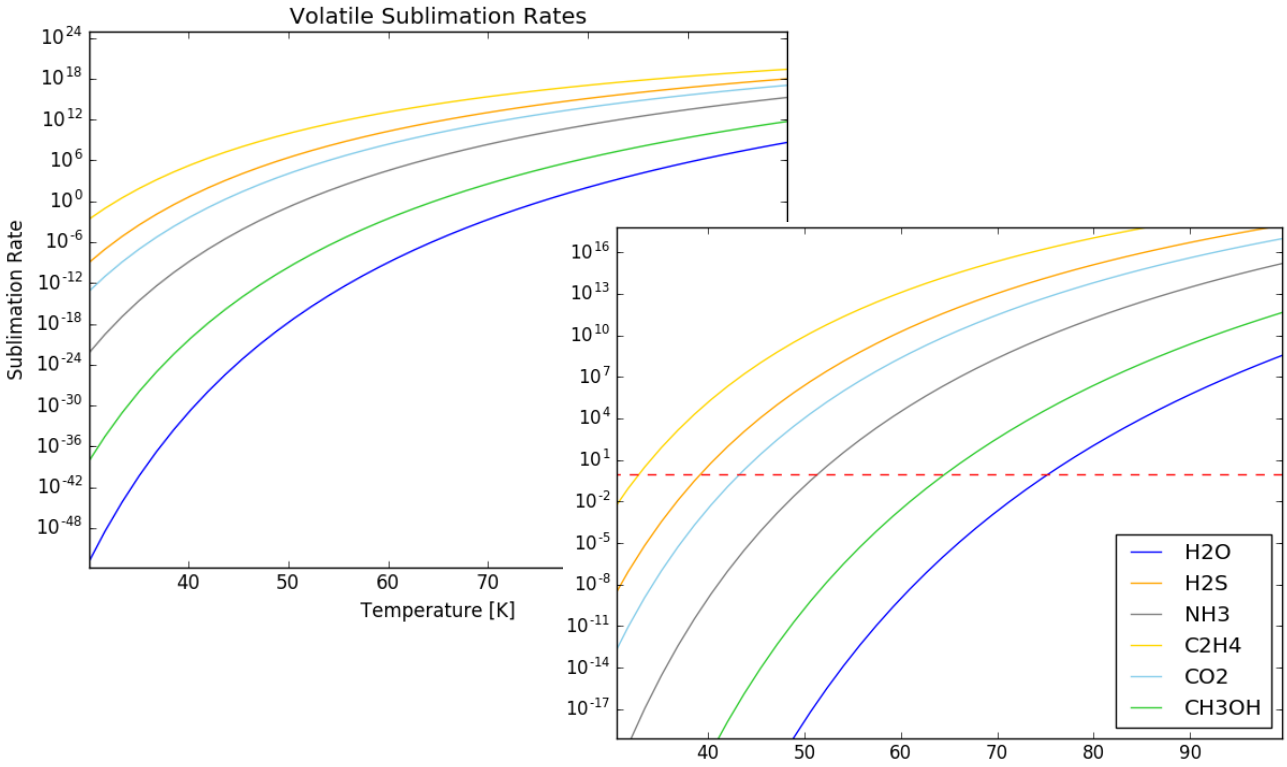

Figure 5.4.1: Sublimation rates of volatiles as a function of surface temperature generated by sections of code found in Appendix A.1. The plot on the right zooms in on the range which sublimation rates fall below 1 molecule per meter squared per second.

Table 5.4: The residence times for simulated volatile species at 50 K, an expected temperature for lunar PSRs.

Species	Residence Time [s]	*Species*	Residence Time [s]
H_2O	2.5 (10^{39})	C_2H_4	4.1 (10^{11})
H_2S	1.4 (10^{15})	CO_2	2.0 (10^{17})
NH_3	3.4 (10^{17})	CH_3OH	1.3 (10^{31})

One can conclude that trapping efficiency is a direct product of photodissociation rate, more so than any other species-based factors. In Figure 5.4.2, one can see that the trapping efficiency is inversely proportional to the photodissociation of individual species. Changing the mass, density or sublimation enthalpy in Figure 5.3.2 did not show any significant change in the number of particles trapped by Cabeus, thus must play minor roles in trapping efficiency. This result helps explain the small amounts of H_2S captured by Cabeus (Figure 5.3.1) as it is the most easily dissociated and thus rarely lasts long enough in transit to be trapped by PSRs.

The prediction of an impactor dominated by H_2S, by Figure 5.3.3, is a result of the poor trapping efficiency compared to other volatiles and its large presence in Cabeus. The model suggests that H_2S is particularly poor at reaching PSRs thus to yield the enhanced abundance in Cabeus the source impactor must have been enriched in H_2S. Conversely, it is more reasonable to suggest there needs to be improvements to the current model. Neither this nor other past works have suggested recombination as a significant factor for volatile concentrations in PSRs. After photodissociation hydrogen ions may escape the lunar system but larger particles can return to the surface. Once settled, it is likely that these heavier elements will recombine with solar wind deposits also on the surface. To simulate this process, one can create another probability

distribution to govern the likelihood of recombination and continued ballistic travel of a particle after photodissociation. Having a recombination rate, based upon the mass of a molecules individual constituents, could lead to hydrogen sulfide and ammonia increasing in trapping efficiency and result in a more typical source volatile ratio.

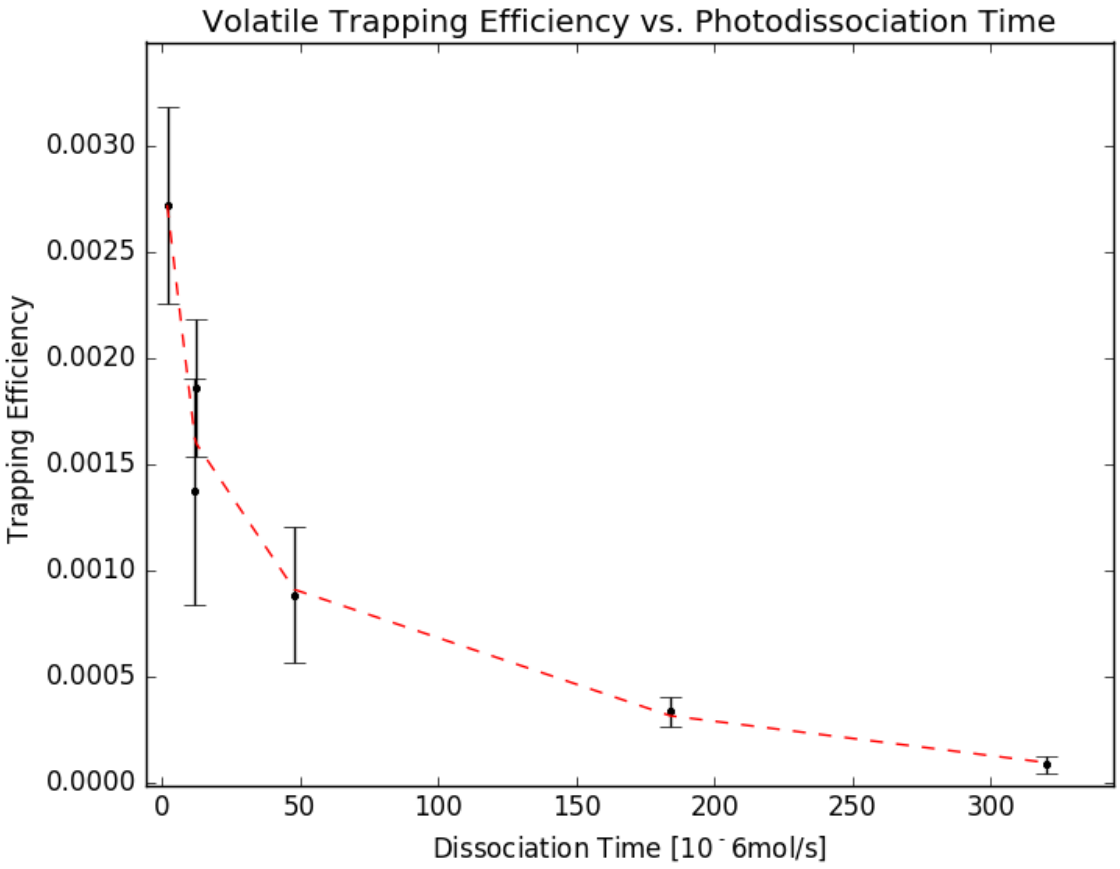

Figure 5.4.2: Volatile trapping efficiency as a function of photodissociation time. Each data point represents a volatile species, error bars are 95% confidence intervals.

Chapter 6

Conclusions

6.1 Conclusions

This work has presented an analysis of lunar volatile trapping in polar PSRs using an exospheric, ballistic transport model. With a uniform distribution across the surface of the Moon, the population of H_2O tracers exhibited a 5.3% trapping rate, a reasonable value when compared to previous work [Schorghofer, 2014][Moores, 2016]. A 5.3% trapping ratio is sufficient to account for the current water ice population, 10^{11} kg, found in lunar polar regions today without the use of a TPW dependent model. Showing that realistic values of water ice can be captured by lunar PSRs, this work supports the hypothesis that a ballistic transport model is sufficient to recreate the current lunar condition. Results also showed volatile concentrations within PSRs peak in the 83° - 86° range due to the lack of PSRs in low-latitude regions (<83°) and the long-time scales needed to reach high-latitude regions (>86°). Drawbacks to this model include the spin up time for the surface temperature to equilibrate and the population of tracers that are abandoned due to the hard stop when simulating the ballistic process.

Furthermore, the simulations of other volatiles gave insight to their behaviour based on physical attributes. This work showed that the photodissociation time of molecules is the strongest contributor to the trapping rate of volatiles. Though this work has served to broaden the knowledge of ballistic transport of various species, there is still room for improvement. By comparing trapping rates of multiple volatile species to the analyses done on the LCROSS impact ejecta plume, these results suggested a source material dominated by hydrogen sulfide. It is apparent that steps should be made to improve this area of research, such as including a recombination process to the current model.

6.2 Future Work

In the future, the selection of PSRs can be increased by including regions less than 10 km in radius; helping to create a more complete and realistic picture of water trapping. This work chose to only take into account 9 south polar PSRs, all of which were less than 5° from the pole, but this subset can easily be increased to 24 by looking at craters up to 10° from the pole, as shown in Figure 6.2.1. By considering PSRs at lower latitudes, one can strengthen or find new trends in the ice concentrations analysed in this work. One can hypothesize that small PSRs can also play a role in volatile trapping. This is because ice residence stability is dependent on energy flux to the sublimation site and this is not directly proportional to the size of the crater. It has been shown that low lying areas with large diameter to depth ratios (D/d) will be exceptional at trapping volatiles as craters with steeper walls can reflect light further into the crater. The claim that larger diameter to depth ratios of craters will result in lower average temperatures is supported by Figure 6.2.2 from Schorghofer et al., 2016 (reproduced below). This is due to energy flux being distributed over larger areas for shallower walls and light reflecting and being absorbed deeper down the crater

less often. In the future, it may be advantageous to focus on PSRs with large D/d ratios. Conversely, trying to identify all PSRs may be time intensive and one can look to replace definite trapping areas with a trapping probability function based on latitude. Using Figure 2.1.2, it is possible to create a probability function to help discern the true ice trapping pattern.

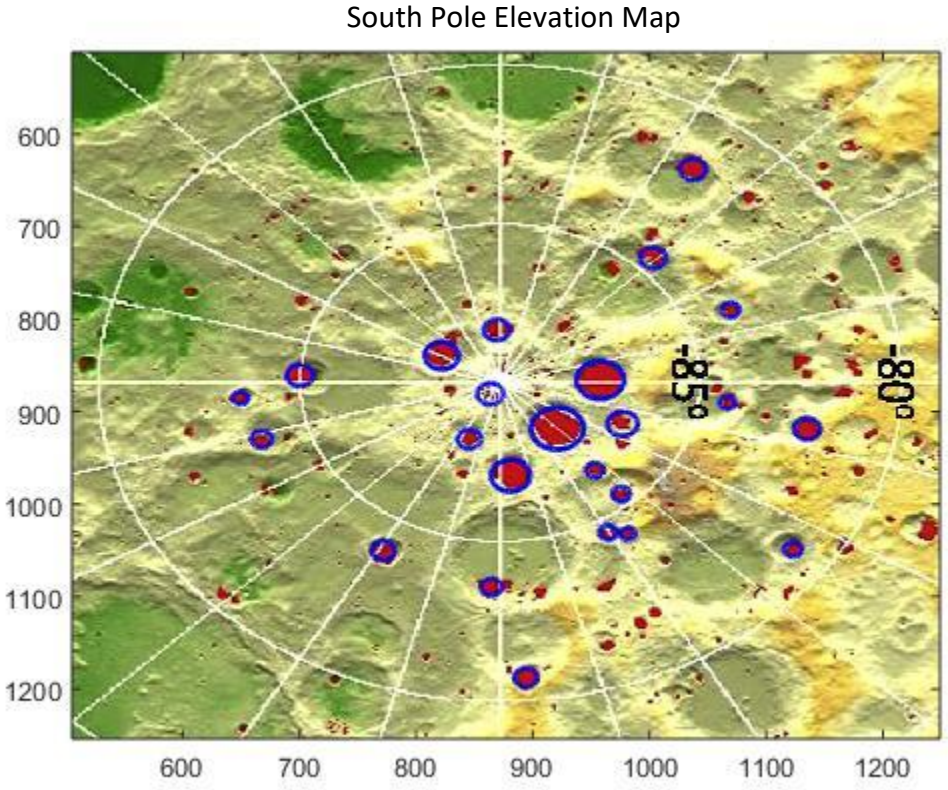

Figure 6.2.1: Map of lunar South pole. The blue rings show other potential PSRs that could be considered using the methods detailed in this paper.

As previously discussed, the species simulations can benefit from a recombination aspect. It is clear that the current model does not accurately depict the processes on the lunar surface. The

recombination of photodissociated heavier particles with hydrogen, implanted by solar winds on the lunar surface, can help constrain the source of lunar surface volatiles.

This model considered the Moon to be a perfectly smooth sphere which neglects the topographical influences for surface temperature calculations. High angle slopes could create temperature fluctuations near the poles, as some areas are under partial shadow and others absorb additional heat. Topography can also affect the flights of particles which may be an interesting aspect to study in future works.

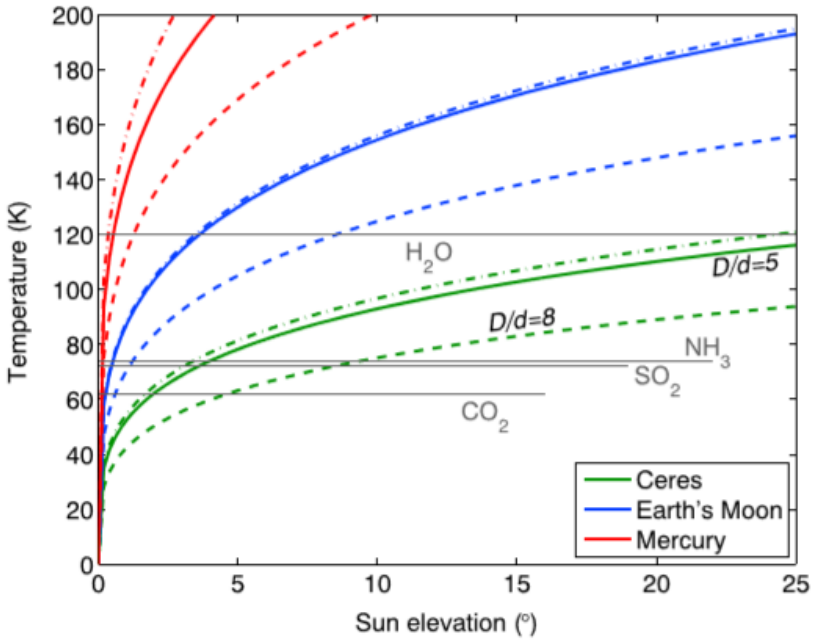

Figure 6.2.2: From Schorghofer, et al., 2016, The sun elevation versus temperature. Lines represent the equilibrium temperature at the bases of craters. Solid lines have diameter to depth ratios of 5 and dashed lines have a ratio of 8.

References

Agnor, C.B., R.M. Canup, and H.F. Levison. On the character and consequences of large impacts in the late stage of terrestrial planet formation. *Icarus,* 142:219, 1999.

Albarède, F. Volatile accretion history of the terrestrial planets and dynamic implications. *Icarus,* 461:1227, 2009.

Arnold, J. Ice in the lunar polar regions, *Journal of Geophysical Research,* 84: 5659, 1979.

Benz, W., W.L. Slattery, and A.G.W. Cameron. The Origin of the Moon and Single-Impact Hypothesis I. *Icarus,* 66:515, 1986.

Boyce, J.W., Y. Liu, G.R. Rossman, Y. Guan, J.M. Eiler, E.M. Stolper, and L.A. Taylor. Lunar apatite with terrestrial volatile abundances. *Nature,* 466:466, 2010.

Butler, B.J. The migration of volatiles on the surfaces of Mercury and the Moon. *Journal of Geophyical. Research,* 102:19,283, 1997.

Campins, H., et al. Water Ice and Organics on the Surface of the Asteroid 24 Themis. *Nature,* 464:1320, 2010.

Canup, R.M., and E. Asphaug. Origin of the Moon in a giant impact near the end of the Earth's formation. *Nature,* 412:708, 2001.

Canup, R.M. Lunar-forming collisions with pre-impact rotation. *Icarus,* 196:518, 2008.

Clark, A., A. Cockett, H. Eisner. The Vapor Pressure of Hydrogen Sulfide. *Proceedings of the Royal Society: Mathematical, Physical and Engineering Sciences,* 209: 408, 1951.

Colaprete, A., et al. Detection of water in the LCROSS ejecta plume. *Science,* 330:463, 2010.

Coombs, D., R. Straube and M.Ward. Diffusion on a sphere with localized traps: mean first passage time, eigenvalue asymptotics, and Fekete points. *Society for Industrial and Applied Mathematics,* 70:302, 2009.

Crank, J., & P. Nicolson. A practical method for numerical evaluation of solutions of partial differential equations of the heat conduction type. *Advances in Computational Mathematics,* 6:207, 1996.

Crovisier, J. The photodissociation of water in cometary atmospheres. *Astronomy and Astrophysics,* 213:459, 1989.

Despois, D., N. Biver, D. Bockelée-Morvan, J. Crovisier. Observations of molecules in comets. *Astrochemistry,* 231:469, 2006.

Feldman, W.C., S. Maurice, A.B. Binder, B.L. Barraclough, R.C. Elphic, and D.J. Lawrence. Fluxes of fast and epithermal neutrons from lunar prospector: Evidence for water ice at the lunar poles. *Science,* 281:1496, 1998.

Giauque, W., C. Egan. Carbon Dioxide. The Heat Capacity and Vapor Pressure of the Solid. The Heat of Sublimation. Thermodynamic and Spectroscopic Values of the Entropy. *Journal of Chemical Physics,* 5:45, 1937.

Gladstone, G.R., et al. Far-ultraviolet reflectance properties of the Moon's permanently shadowed regions. *Journal of Geophysical Research,* 117: E00H04, 2012. Greenwood, J.P., S. Itoh, N. Sakamoto, P. Warren, L. Taylor and H. Yurimoto. Hydrogen isotope ratios in lunar rocks indicate delivery of cometary water to the Moon. *Nature Geoscience,* 4:79, 2011.

Hartmann, W.K., and D.R. Davis. Satellite-sized planetesimals and lunar origin. *Icarus,* 24:504, 1975.

Hayne, P.O., A. Hendrix, E. Sefton-Nash, M.A. Siegler, P.G. Lucey, K.D. Retherford, J.P. Williams, B.T. Greenhagen, and D.A. Paige. Evidence for exposed water ice in the Moon's south polar regions from Lunar Reconnaissance Orbiter ultraviolet albedo and temperature measurements. *Icarus,* 255:58, 2015.

Hodges, R. R. Jr Ice in the lunar polar regions revisited, *Journal of Geophysical Research*, 107: 5011, 2002.

Jacobsen, S., et al. The isotopic composition of the lunar crust and the age and origin of the moon: evidence from lunar soils. *41st Lunar and Planetary Science Conference,* 2596, 2010.

Kegerreis, J.A., et al. Evidence for a Localized Source of the Argon in the Lunar Exosphere. *Joural of Geophysical Research,* 122:2163, 2017.

Lugmair, G.W., and Shukolyukov, A. Early solar system timescales according to 53Mn- 53Cr systematics. *Elsevier,* 62:2863, 1998.

Meeus, J. Mathematical and Astronomy Morsels, 1997.

Mitrofanov, I.G., et al. Hydrogen Mapping of the Lunar South Pole Using the LRO Neutron Detector Experiment LEND. *Science,* 330:483, 2010.

Mitrofanov, I.G., et al. Testing polar spots of water-rich permafrost on the Moon: LEND observations onboard LRO. *Journal of Geophysical Research,* 117: E00H27, 2012.

Moores, J.E. Lunar water migration in the interval between large impacts: Heterogeneous delivery to Permanently Shadowed Regions, fractionation, and diffusive barriers. *Journal of Geophyical. Research: Planets,* 121:46, 2016.

McGovern, J.A., D.B. Bussey, B.T. Greenhagen, D.A. Paige, J.T.S. Cahill, and P.D. Spudis. Mapping and characterization of non-polar permanent shadows on the lunar surface. *Icarus,* 223:566, 2013.

Ong, L., E. Asphaug, D. Korycansky R. Coker. Volatile retention from cometary impacts on the Moon, *Icarus,* 207: 578, 2010.

Overstreet, R., W. Giauque. Ammonia. The Heat Capacity and Vapor Pressure of Solid and Liquid. Heat of Vaporization. The Entropy Values from Thermal and Spectroscopic Data. *Journal of American Chemistry Society,* 59: 254, 1937.

Paige, D.A., et al. Diviner Lunar Radiometer observations of cold traps in the Moon's south polar region. *Science,* 330:479, 2010.

Rivkin, A., J. Emery. Detection of Ice and Organics on an Asteroidal Surface. *Nature*, 464: 1322, 2010.

Saal, A.E., E.H. Hauri, M.L. Cascio, J.A. Van Orman, M.C. Rutherford, and R.F. Cooper. Volatile content of lunar volcanic glasses and the presence of water in the Moon's interior. *Nature*, 454:192, 2008.

Schorghofer, N., G.J. Taylor. Subsurface migration of H2O at lunar cold traps. *Journal of Geophysical Research*, 112, 2007.

Schorghofer, N. Migration calculations for water in the exosphere of the Moon: Dusk-dawn asymmetry, heterogeneous trapping and D/H fractionation. *Geophysical Research Letters*, 41:4888, 2014.

Schorghofer, N., et al. The permanently shadowed regions of dwarf planet Ceres. *Geophysical Research Letters*, 43:6783, 2016.

Siegler, M.A., et al. Lunar true polar wander inferred from polar hydrogen. *Nature*, 531:480, 2016.

Sridharan,R., et al. 'Direct' evidence for water (H2O) in the sunlit lunar ambience from CHACE on MIP of Chandrayaan I. *Planetary and Space Science*, 58:947, 2010.

Sunshine, J.M., et al. Temporal and Spatial Variability of Lunar Hydration As Observed by the Deep Impact Spacecraft. *Science*, 326:565, 2009.

Taylor, S.R., G.J. Taylor, and L.A. Taylor. The Moon: A Taylor perspective. *Icarus*, 70:5904, 2006.

Tickner, A., F. Lossing. The Measurement of Low Vapor Pressures by Means of a Mass Spectrometer. *Journal of Physical Chemistry,* 55: 733, 1951.

Vasavada, A., et al. Lunar equatorial surface temperatures and regolith properties from the Diviner Lunar Radiometer Experiment. *Journal of Geophysical Research,* 117, 2012.

Watson, K., B. C. Murray, and H. Brown. On the possible presence of ice on the Moon. *Journal of Geophysical Research,* 66:1598, 1961a.

Watson, K., B. C. Murray, and H. Brown. The behavior of volatiles on the lunar surface. *Journal of Geophysical Research,* 66:3033 ,1961b.

Appendices

A.1 Ballistic Hopping

Detailed below is the bulk of the ballistic hopping section of code written in Python 2.7. Functions: psv and sublrate implement equations 4 and 3 respectively. These are used by function: res_time to find the residence time of particles based on lunar surface temperature. Function: hop1 calculates a particle's new position based on its position on the moon and the temperature of the surface at that point. In the case that a particle's speed reaches 40% of escape velocity, function: nonunigrav takes in the speed and angle of trajectory to determine the landing position. This function takes into consideration that these particles are moving fast enough that the curvature of the body will affect the direction gravity is pulling said particle. Once landed function: incoldtrap checks to see if the particle has landed within a list of PSRs, if so – after recording the result - function: production will reset the particle. Note, function: production also resets particles that are photodissociated or have escaped the system this; meaning new particles will continue being simulated as the originals ultimately reach their termination.

```
def psv(T):
    R = 8.314
    pt=6.11e2
    Tt=273.16
```

```
    C=(DHsub/R)*(1./T - 1./Tt)
    return pt*exp(-C)

def sublrate(T):
    kB = 1.38065e-23
    mu=mass*1.66054e-27
    return psv(T)/sqrt(2*pi*kB*T*mu)

def res_time(T):
    sigma0=(dens/(mass/6e23))**(2./3)*1e4
    res_time=sigma0/sublrate(T)
    res_time *=400.
    if T==0.: res_time = 1e32
    return res_time

def nonunigrav(vspeed,alpha):
    gamma = (vspeed/vesc)**2
    a = Rbody/2./(1-gamma)
    ecc = sqrt(1-4*(1-gamma)*gamma*sin(alpha)**2)
    d = 2*Rbody*arccos(1/ecc*(1-2*gamma*sin(alpha)**2))
    Ep = pi - 2*arctan(sqrt((1-ecc)/(1+ecc))/tan(d/(4*Rbody)))
    if ecc > 1. - 1e-5:
        d = Rbody*4*gamma*sin(alpha)
        Ep = pi - 2*arctan(sqrt((1-gamma)/gamma))

    t = 2*sqrt(2*a**3/Rbody/vesc**2)*(Ep+ecc*sin(Ep))
    if 1 -2*gamma*sin(alpha)**2 > ecc:
```

```
        d = 0
        t = 0
    return d, t

def hop1(pr,ps,pt,Tsurf,Q):
    v = zeros(3)
    buf=sqrt(Tsurf*8314.5/mass)
    v[0] = random.normal()*buf
    v[1] = random.normal()*buf
    v[2] = abs(random.normal())*buf
    vspeed = sqrt(sum(v**2))

    if vspeed > vesc :
        ps = -2
        pt = 1e100

    flighttime = 2*v[2]/g
    d=flighttime*sqrt(v[0]**2+v[1]**2)

    if vspeed > 0.4*vesc:
        alpha = arctan(sqrt(v[0]**2+v[1]**2)/v[2])
        d,flighttime = nonunigrav(vspeed, alpha)
    az=arctan2(v[1],v[0])
    cosaz = v[1]/sqrt(v[0]**2+v[1]**2)
    lat = pr[1]*d2r
    sinph2 = sin(d/Rbody)*cos(lat)*cosaz + sin(lat)*cos(d/Rbody)
    pr[1] = arcsin(sinph2)/d2r
```

```
    cosph2 = sqrt(1.-sinph2**2)

    if cosph2 != 0 :
        cosdlon = (cos(d/Rbody)*cos(lat)-
sin(lat)*sin(d/Rbody)*cosaz)/cosph2

        if cosdlon > 1. :
            cosdlon = 1.
        if cosdlon < -1. :
            cosdlon = -1.
        dlon = arccos(cosdlon)
        if v[0] < 0. :
            dlon = -dlon
        pr[0] += dlon/d2r
    else: pr[0] = 0.

    if abs(pr[1]) > 90. :
        print 'hop1: this cannot happen', pr[1]

    pr[0] %= 360
    ps=1
    pt +=flighttime

    if Q>0. and tau > 0:
        u = rand()
        destr_rate = flighttime/(tau*semia**2)
        if u < destr_rate :
            ps=-1
```

```
            pt=1e100
    hopdistances.append(sqrt(sum((before-after)**2)))
    return pr,ps,pt


def incoldtrap(pr):
    if min(((pr[0]*ones(len(Craters))-
Craters[:,0])*abs(cos(pi/180.*Craters[:,1])))**2 +
(pr[1]*ones(len(Craters))-Craters[:,1])**2 - Craters[:,2]**2) <
0:
        return True
    else:
        return False


def production(Np,pr,ps,pn,Tsurf):
    NPROD = 2000
    newcc=0
    for i in arange(Np):
        if ps[i] < 0 :
            ps[i] = 0
            pn[i] = 0
            pr[i,0]= 360.*rand()
            pr[i,1]= 180/pi*arccos(2*rand()-1)-90
            k=inbox(pr[i])
            if Tsurf[k]>360.:
                break
            newcc +=1
        if newcc == NPROD:
            break
```

```
    return pr, ps, pn, newcc
```

A.2 Temperature Profile

Detailed below is the bulk of the surface temperature section of code written in Python 2.7. Function: flux_noatm is the energy or heat flux coming from the sun based on the distance from the Sun and its position in the sky for each line of latitude on the Moon's surface. Function: conduction is where we calculate how the heat is passed through the layers of the Moon. Each point is dependant on incoming flux from the Sun and heat conducted from neighbouring points. Function: SurfaceTemperature is the application of the previous two function to create a surface temperature profile. This profile is what drives ballistic transport of lunar volatiles. It should be clear that the distribution of heat through conduction is slow, and thus there is a spin up time for the surface temperature to reach an equilibrium. This section of code runs for 10 lunations before any ballistic transport is introduced.

```
def flux_noatm(R,decl,latitude,HA,surfaceSlope,azFac):
#energy/heat flux
    So=1365.
    c1=cos(latitude)*cos(decl)
    s1=sin(latitude)*sin(decl)
    sinbeta = c1*cos(HA) + s1
    cosbeta = sqrt(1-sinbeta**2)
    buf = (sin(decl)-
sin(latitude)*sinbeta)/(cos(latitude)*cosbeta)
```

```
    if buf < 1. :
        buf= 1.
    if buf  < -1 :
        buf = -1.
    azSun = arccos(buf)
    if sin(HA)>=0 :
        azSun=2*pi-azSun
    sintheta = cos(surfaceSlope)*sinbeta +
sin(surfaceSlope)*cosbeta*cos(azSun-azFac)
    if cosbeta==0.:
        sintheta = cos(surfaceSlope)*sinbeta
    sintheta = max(sintheta,0)
    if sinbeta < 0. :
        sintheta = 0.
    flux_noatm = sintheta*So/(R**2)
    return flux_noatm



def
conductionQ(nz,z,dt,Qn,Qnp1,T,ti,rhoc,emiss,Tsurf,Fgeotherm):
#used for surface temp
    nmax=1000
    sigSB=5.67051e-8
    k=ones(nz)
    alpha=ones(nz)
    gamma=ones(nz)
    a=ones(nz)
    b=ones(nz)
```

```
    c=ones(nz)
    r=ones(nz)

    k=ti**2./rhoc
    dz=2.*z[0]
    beta = dt/rhoc[0]/(2*dz**2)
    alpha[0] = beta*k[1]
    gamma[0] = beta*k[0]
    for i in arange(1,int(nz-1)):
        buf=dt/(z[i+1]-z[i-1])
        alpha[i] = 2.*k[i+1]*buf/(rhoc[i]+rhoc[i+1])/(z[i+1]-
z[i])
        gamma[i] = 2.*k[i]*buf/(rhoc[i]+rhoc[i+1])/(z[i]-z[i-1])
    buf=dt/(z[nz]-z[nz-1])**2

    gamma[nz-1] = k[nz-1]*buf/(2.*rhoc[nz-1])
    k1=k[0]/dz
    a=-gamma
    b = 1. +alpha +gamma
    c = -alpha
    b[nz-1] = 1.+ gamma[nz-1]
    Tr=Tsurf
    arad = -3.*emiss*sigSB*Tr**4
    brad = 2.*emiss*sigSB*Tr**3
    ann = (Qn-arad)/(k1+brad)
    annp1 = (Qnp1-arad)/(k1+brad)
    bn = (k1-brad)/(k1+brad)
    b[0] = 1. + alpha[0] + gamma[0] -gamma[0]*bn
```

```
    r[0] = gamma[0]*(annp1+ann)+(1.-alpha[0] - gamma[0]
+gamma[0]*bn)*T[0] +alpha[1]*T[1]

    for i in arange(1,int(nz-1)):

        r[i] = gamma[i]*T[i-1] + (1.-alpha[i]-gamma[i])*T[i]+
alpha[i]*T[i+1]

    r[nz-1] = gamma[nz-1]*T[nz-2] + (1.+gamma[nz-1])*T[nz-1] +
dt/rhoc[nz-1]*Fgeotherm/(z[nz-1]-z[nz-2])

    T = tridag(a,b,c,r,T,nz)

    Tsurf = 0.5*(annp1 + bn*T[0] + T[0])

    if Tsurf<=0.:

        Tsurf=1.

    return Tsurf, T


def SurfaceTemperature(dtsec, HAi, time, Tsurf, Qn, z):

    global Fcall

    sigSB=5.6704e-8

    zero=0.

    nz=30.

    zfac=1.07e0

    decl=0

    sunR=semia

    thIn=50. #I=sqrt(k*rho*c)

    rhoc=1000000.

    ti=zeros(nmax)

    rhocv=zeros(nmax)

    ti[:nz] = thIn

    rhocv[:nz] = rhoc

    if Fcall == True:
```

```
        delta = thIn/rhoc*sqrt(solarDay/pi)
        print 'Thermal model parameters:'
        print 'nz=',nz,' zmax=',zmax,' zfac=',zfac
        print 'Thermal inertia=',thIn,' rho*c=',rhoc
        print 'Geothermal flux=',Fgeotherm
        print 'Diurnal skin depth=',delta
        print 'Albedo=',albedo

        z=setgrid(nz,z,zmax,zfac)
        for k in arange(int(veclen)):
            lon, lat = k2lonlat(k)
            geof=cos(lat)/pi
            Tmean=(1370*(1.-albedo)*geof/sigSB)**0.25 - 10.
            if Tmean <= 0:
                Tmean=(Fgeotherm/sigSB)**0.25
            T[:,k]=Tmean
            Tsurf[k]=Tmean
            HA=2.*pi*((time-dtsec)/solarDay+(lon-HAi)/360.%1.)
            Qn[k]=(1-
albedo)*flux_noatm(sunR,decl,lat,HA,zero,zero)

    for k in arange(int(veclen)):
        lon, lat = k2lonlat(k)
        HA=2.*pi*(time/solarDay+(lon-HAi)/360.%1.)
        Qnp1=(1-albedo)*flux_noatm(sunR,decl,lat,HA,zero,zero)
        Tsurf[k], T[:,k] = conduction (nz, z, dtsec, Qn[k],
Qnp1, T[:,k], ti, rhocv, emiss, Tsurf[k], Fgeotherm)
```

```
        Qn[k]=Qnp1
    return Tsurf, Qn, ti, rhocv, z,T
```

A.3 Glossary

Adsorption – The adhesion of gas or liquid (adsorbate) molecules to a surface (adsorbent)

Bond Albedo – the fraction of incident light that is reflected back into space, over all wavelengths and phase angles

LCROSS - The Lunar Crater Observation and Sensing Satellite was a spacecraft sent to determine the nature of hydrogen near the lunar poles.

LEND – The Lunar Exploration Neutron Detector is an instrument on board the LRO which creates hydrogen distribution maps of the surface of the Moon.

LRO – The Lunar Reconnaissance Orbiter is a spacecraft orbiting the moon which collects detailed mapping data via instruments on board.

Lunation – refer to "synodic month"

Synodic month – The time it takes for the moon to reach the same position relative to the Earth and the Sun, this is approximately 29.53 days and is slightly longer than a sidereal month which is taken in respect to background stars.

TPW – True Polar Wander is a rotation of a celestial body with respect to its spin axis, causing the geographic locations of the north and south poles to change.

Photodissociation – the separation or splitting of a chemical compound by photons.

PKT - The Procellarum KREEP Terrane is a large area on the near side of the moon abundant in potassium (K), rare earth elements (REE) and phosphorus (P).

PSR – Permanently Shadowed Regions are areas that never receive sunlight due to shadows cast by the surrounding topography.

Transient Atmosphere - A transient exosphere is an atmosphere that fluctuates in density during day light and night time hours. Most commonly found on small bodies. The incoming heat sublimates volatiles on the surface during the day adding to the active atmosphere which will diminish at night as the temperature decreases and volatiles once again freeze onto the surface.

Volatile – a compound that easily transitions into a gas